



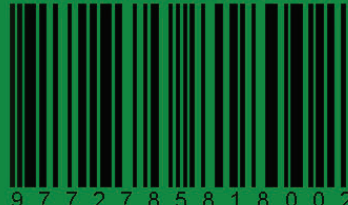
Asian Journal of

Electrical and Electronic Engineering

VOLUME 3 ISSUE 1 MARCH 2023



eISSN 2785-8189



9 7 7 2 7 8 5 8 1 8 0 0 2

<https://alambiblio.com/ojs/index.php/ajoeee>

COPYRIGHT NOTICE

Consent to publish: The Author(s) agree to publish their articles with AlamBiblio Press.

Declaration: The Author(s) declare that the article has not been published before in any form. It is not concurrently submitted to another publication and does not infringe on anyone's copyright. The author (s) holds the AlamBiblio Press and Editors of the Journal harmless against all copyright claims.

Transfer of copyright: The Author(s) hereby agree to transfer the article's copyright to **AlamBiblio Press**, which shall have the non-exclusive and unlimited right to publish the article in any form, including in electronic media. For articles with more than one author, the corresponding author confirms that he/she is authorized by his/her co-author(s) to grant this transfer of copyright.

The Asian Journal of Electrical and Electronic Engineering Journal follows the open access policy.

All articles published with open access will be immediately and permanently free for everyone to read, download, copy and distribute.

ASIAN JOURNAL OF ELECTRICAL AND ELECTRONIC ENGINEERING

eISSN 2785-8189



Published by:

AlamBiblio Press,
PV8 platinum Hill
Jalan Melati Utama, 53100 Kuala Lumpur, Malaysia
Phone (+603) 2713 7308

Whilst the publisher and editorial board make every effort to see that no inaccurate or misleading data, opinion or statement appears in this Journal, they wish to make it clear that the data and opinions appearing in the articles and advertisements herein are the responsibility of the contributor or advertiser concerned. Accordingly, the publisher and the editorial committee accept no liability whatsoever for the consequence of any such inaccurate or misleading data, opinion or statement.



This work is licensed under a Creative Commons Attribution-Non-Commercial 4.0 International License.



CHIEF EDITOR

Prof. Dr. AHM Zahirul Alam, IIUM, Malaysia

EXECUTIVE EDITOR

Assoc. Prof. Dr. Muhammad Mahbubur Rashid, IIUM, Malaysia

EDITORIAL BOARD MEMBERS

Prof. Dr. Sheroz Khan
Onaizah College of Engineering and Information Technology
Saudi Arab

Prof. Dr. AHM Asadul Huq
Department of Electrical and Electronic Engineering
Dhaka University, Bangladesh

Prof. Dr. Pran Kanai Shaha
Department of Electrical and Electronic Engineering
Bangladesh University of Engineering and Technology,
Bangladesh

Assoc. Prof. Dr. SMA Motakabber
Faculty of Engineering
International Islamic University Malaysia, Malaysia

Prof. Dr. ABM Harun Ur Rashid
Department of Electrical and Electronic Engineering
Bangladesh University of Engineering and Technology,
Bangladesh

Prof. Dr. Joarder Kamruzzaman
Engineering and Information Technology
Federal University, Australia

Assoc. Prof. Dr. Md Arafatur Rahman
Faculty of Computing
Universiti Malaysia Pahang

AIMS & SCOPE OF THE ASIAN JOURNAL OF ELECTRICAL AND ELECTRONIC ENGINEERING

The **Asian Journal of Electrical and Electronic Engineering (AJoEEE)**, published biannually (March and September), is a peer-reviewed open-access journal of the **AlamBiblio Press**.

The Asian Journal of Electrical and Electronic Engineering publishes original research findings as regular papers and review papers (by invitation). The Journal provides a platform for Engineers, Researchers, Academicians, and Practitioners who are highly motivated to contribute to the Electrical and Electronics Engineering disciplines. It also welcomes contributions that address the developing world's specific challenges and address science and technology issues from a multidisciplinary perspective.

REFEREES' NETWORK

All papers submitted to AJoEEE Journal will be subjected to a rigorous reviewing process through a worldwide network of specialized and competent referees. Each accepted paper should have at least two positive referees' assessments.

SUBMISSION OF A MANUSCRIPT

A manuscript should be submitted online to the Asian Journal of Electrical and Electronic Engineering (AJoEEE) website <https://alambiblio.com/ojs/index.php/ajoeee>. Further correspondence on the status of the paper could be done through the journal website

Volume 3, Issue 1, March 2023

TABLE OF CONTENTS

| | |
|---|----|
| COPYRIGHT NOTICE | i |
| EDITORIAL..... | ii |
| ARTICLES | |
| DIRECT TORQUE CONTROL OF THREE PHASE INDUCTION MOTORS: CONCEPT & PRINCIPLES..... | 1 |
| <i>Ayman M. Ali, M. Abdel Latif Badr and Hosain Farid S</i> | |
| TECH STOCKS AND DIVIDEND POLICY IN MALAYSIA | 16 |
| <i>Ahmad Ibn Ibrahimy and Saad Bin Amjad</i> | |
| DUAL-ADAPTIVE REDUNDANCY MINIMISATION-BASED CHANNEL ESTIMATION METHOD FOR MIMO OFDM SYSTEMS | 20 |
| <i>Ahmad Hasan, S. M. A. Motakabber and AHM Zahirul Alam</i> | |
| NOISE REDUCTION TECHNIQUES IN ECG SIGNAL | 27 |
| <i>Sakarie M. Muhumed, and Muhammad I. Ibrahimy</i> | |
| EFFECT OF INDUCTOR FOR DESIGNING AN INVERTER TO MAXIMIZE SOLAR PANEL POWER OUTPUT | 34 |
| <i>Muhammad Wasif Hasan and AHM Zahirul Alam</i> | |

Direct Torque Control of Three Phase Induction Motors: Concept & Principles

Ayman M. Ali^{1*}, M. Abdel Latif Badr², Hosain Farid S.²

¹Aircraft Systems Engineer, EgyptAir M&E, Ph.D. of Electrical Engineering, Cairo, Egypt

²Prof. of Electric Power & Machines, Faculty of Engineering, Ain shams University, Cairo, Egypt

*Corresponding author: aymnaly@yahoo.com

(Received: 11 September 2022; Accepted: 23 September 2023)

Abstract— This paper thoroughly illustrates the Direct Torque Control (DTC) concept, principles and theory. It describes the dynamic behavior of a direct torque controlled three-phase induction motor. The complete analysis begins with a suitable mathematical model of the motor and the inverter circuit. It represents the DTC main parts and describes its operation. This paper also illustrates how the DTC can become a base for speed control schemes and the ability to switch between torque & speed control.

Keywords: Direct Torque Control, DTC, Flux Vector Control, 3-phase Induction Motor, Motor Control, Variable Speed Drive

1. INTRODUCTION

Direct Torque Control (DTC) is one of the latest developments in ac motor control. It provides high torque dynamic response. DTC almost re-establishes dc drive advantages through direct torque and flux control implementation, which electrical engineers and researchers were looking for. Since its introduction in 1985, the DTC principle has been widely applied to fast dynamic induction motor drives. Despite DTC's simplicity, it can produce very fast flux and torque control. And if the flux and torque are accurately estimated, DTC is almost unaffected by motor parameters and perturbations. However, notable flux, torque and current pulsations occur during steady-state motor operation [1].

Regarding induction motor control, the intention is directed to control its output quantities, namely torque and speed. Induction motor speed control is more famous than torque control. However, industrial applications need torque control as well as speed control in some cases. Also, torque control can be used as a base to speed control.

2. THREE-PHASE INDUCTION MOTORS MATHEMATICAL MODEL

The space vector concept, also called space phasor, has been used in the ac motor drives analysis since it is more suitable for investigating the dynamic behaviour of the motor. The basic idea of this concept is to transform the instantaneous three-phase machine variables such as voltages, fluxes and currents to space vectors onto a complex plane located in the motor cross-section. In this plane, the space phasor rotates with an angular speed equal to the angular frequency of the three-phase supply with respect to the fixed (stationary) reference frame [2, 1].

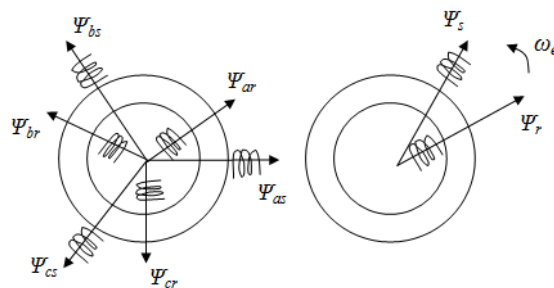


Fig. 1. Space phasor of induction motor rotating fields

Fig. 1 illustrates how the flux linkage space vector, which rotates in the machine space along the air gap periphery, represents the three-phase time-varying fluxes.

2.1 Dynamic Model in Space Vector Form

For a three-phase induction motor, the space vector \mathbf{Y} of the stator current, Flux or voltage is defined from its phase quantities by:

$$\mathbf{Y} = (2/3) [Y_a(t) + a \cdot Y_b(t) + a^2 \cdot Y_c(t)] \quad (1)$$

where $a = \exp(j2\pi/3)$, note that space vectors are denoted as **boldface** letters.

The above transform is reversible, and each phase quantity can be calculated from the space vector by:

$$Y_a = \text{Re}(\mathbf{Y}), Y_b = \text{Re}(a^2 \cdot \mathbf{Y}), Y_c = \text{Re}(a \cdot \mathbf{Y}). \quad (2)$$

where $\text{Re}(\mathbf{Y})$ and $\text{Im}(\mathbf{Y})$ are the real and imaginary values of a space vector \mathbf{Y} .

With space vector notation, we can deduce the dynamic model and equivalent circuit of the induction motor referred to the stationary reference frame (fixed to stator) as follow [3]:

Voltage equations on the stator and rotor circuits are:

$$\mathbf{V}_s = R_s \mathbf{I}_s + D \mathbf{\Psi}_s \quad (3)$$

$$\mathbf{V}_r' = R_r' \mathbf{I}_r' + D \mathbf{\Psi}_r' = 0 \quad (4)$$

where “ D ” is the derivative operator w.r.t. time (d/dt) and \mathbf{V} , \mathbf{I} and $\mathbf{\Psi}$ are motor voltage, current and flux linkage, respectively and subscripts “ s , r ” donate stator and rotor quantities. Primed quantities are stator and rotor variables referred to as their reference frames. Usually, actual rotor variables (\mathbf{V}_r' , \mathbf{I}_r' , $\mathbf{\Psi}_r'$) of Eq.(4), which are computed in the rotor reference frame, is transformed into new variables (\mathbf{V}_r , \mathbf{I}_r , $\mathbf{\Psi}_r$) referred to stator reference frame as in the conventional steady-state equivalent circuit derivation. Let the stator to rotor winding turns ratio be “ n ” and the angular position of the rotor be “ θ ”, and let us define:

$$\mathbf{I}_r = (1/n) \exp(j\theta) \mathbf{I}_r' \quad , \quad \mathbf{\Psi}_r = n \exp(j\theta) \mathbf{\Psi}_r' \quad (5)$$

where “ j ” is the complex operator. Also, by defining referred rotor impedances as $R_r = n^2 R_r'$, $L_l_r = n^2 L_l_r'$, we can rewrite Eq.(4) referred to stator reference frame as:

$$0 = R_r \mathbf{I}_r + (D - j\omega_o) \mathbf{\Psi}_r \quad (6)$$

$$0 = R_r \mathbf{I}_r + D \mathbf{\Psi}_r - j\omega_o \mathbf{\Psi}_r \quad (7)$$

where $\omega_o = D \theta_o$, is the speed of the motor in electrical frequency units, so the term $(\omega_o \mathbf{\Psi}_r)$ is called speed voltage drop, which expresses the power conversion. Also, the flux linkages can be expressed as:

$$\mathbf{\Psi}_s = L_s \mathbf{I}_s + L_m \mathbf{I}_r \quad (8)$$

$$\mathbf{\Psi}_r = L_m \mathbf{I}_s + L_r \mathbf{I}_r \quad (9)$$

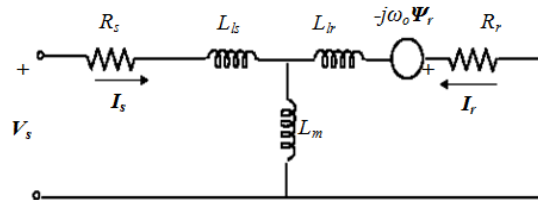


Fig. 2. Dynamic equivalent circuit referred to the stationary reference frame

The four equations Eqs.(3, 6, 8 & 9) constitute an induction motor dynamic model referred to as stationary (stator) reference frame in space phasor form. By eliminating flux linkages, model equations can be simplified as follows:

$$\mathbf{V}_s = (R_s + L_s D) \mathbf{I}_s + L_m D \mathbf{I}_r \quad (10)$$

$$0 = [R_r + L_r (D - j\omega_o)] \mathbf{I}_r + L_m (D - j\omega_o) \mathbf{I}_s \quad (11)$$

By restoring the speed voltage term in the previous equation, we obtain Eq.(12):

$$0 = (R_r + L_r D) \mathbf{I}_r + L_m D \mathbf{I}_s - j \omega_o \Psi_r \quad (12)$$

From Eqs.(10, 12), the model of dynamic equivalent circuit referred to stationary reference frame can be drawn as in Fig. 2. With excitation frequency ω_e at steady state operation, the derivative operator D in Eqs.(10, 11) is replaced by $j\omega_e$ and after some algebraic rearrange, we will get:

$$\mathbf{V}_s = (R_s + j\omega_e L_s) \mathbf{I}_s + j\omega_e L_m \mathbf{I}_r \quad (13)$$

$$0 = (R_r/s + j\omega_e L_r) \mathbf{I}_r + j\omega_e L_m \mathbf{I}_s \quad (14)$$

Those entirely describe the famous and conventional steady-state equivalent circuit. The above-mentioned procedure is general and accordingly, the dynamic model may be described in any arbitrary reference frame rotating at speed ω_a . The previous analysis, the stator reference frame, is a special case of the general one with $\omega_a = 0$. In the case of the analysis referred to the rotor reference frame, we have $\omega_a = \omega_o$. In the case of the analysis with respect to the synchronously rotating reference frame, we have $\omega_a = \omega_e$ [3]. In the present case, direct torque control, the analysis with respect to the stationary reference frame is suitable and enough. Generally, the suitable choice of reference frame is significant for simplifying motor analysis and control.

2.2 d-q Equivalent Circuit

Often, induction motors analysis with a space vector model is complicated because we have to deal with complex number variables. For any space phasor or vector \mathbf{Y} , two real quantities Y_q and Y_d can be defined as follows:

$$\mathbf{Y} = Y_q - j Y_d \quad (15)$$

In other words, $Y_q = \text{Re}(\mathbf{Y})$ and $Y_d = -\text{Im}(\mathbf{Y})$. Fig. 3 illustrates how the d-q axes are defined on a stationary reference frame at a certain angle with respect to a-b-c frame. This angle is equal to zero in our analysis (the q-axis lies on the a-axis, which is taken as a reference).

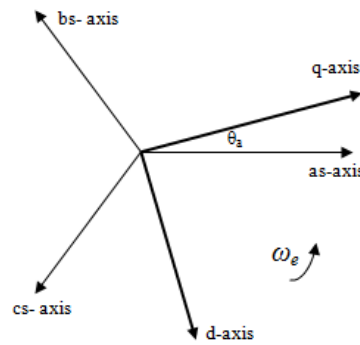


Fig. 3. d and q axes definition on an arbitrary reference frame

As mentioned before, the space vector \mathbf{Y} represents voltage, current or Flux linkage. With the above definition in Eq.(15), Eqs. (10, 11) can be translated into the following four equations of real variables as follow:

$$V_{qs} = (R_s + L_s D) I_{qs} + L_m D I_{qr} \quad (16)$$

$$V_{ds} = (R_s + L_s D) I_{ds} + L_m D I_{dr} \quad (17)$$

$$0 = L_m D I_{qs} - \omega_o L_m I_{ds} + (R_r + L_r D) I_{qr} - \omega_o L_r I_{dr} \quad (18)$$

$$0 = -\omega_o L_m I_{qs} + L_m D I_{ds} - \omega_o L_r I_{qr} + (R_r + L_r D) I_{dr} \quad (19)$$

Also Eq.(12) can be translated into the following two equations:

$$0 = (R_r + L_r D) I_{qr} + L_m D I_{qs} - \omega_o \Psi_{dr} \quad (20)$$

$$0 = (R_r + L_r D) I_{dr} + L_m D I_{ds} + \omega_o \Psi_{qr} \quad (21)$$

Based on Eqs. (16, 17, 20 & 21), the d-q equivalent circuit, referred to the stator reference frame, can be drawn as shown in Fig. 4.

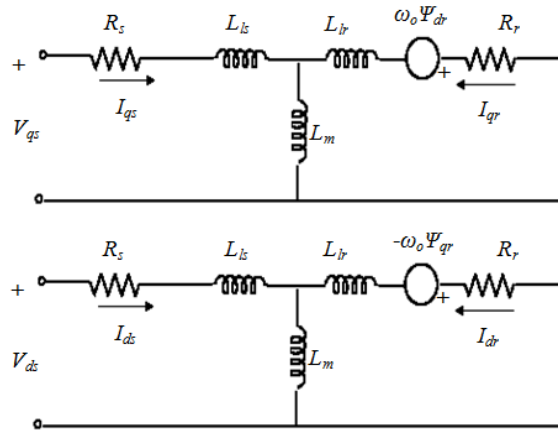


Fig. 4. d-q equivalent circuit referred to the stationary reference frame

Another set of equations, including flux linkage variables, is required to explain the DTC concept. By translating Eqs. (3, 6, 8 & 9) in d-q coordinates on the stator frame, we have the following eight equations:

- Stator and rotor voltage equations:

$$V_{qs} = R_s I_{qs} + D \Psi_{qs} \quad (22)$$

$$V_{ds} = R_s I_{ds} + D \Psi_{ds} \quad (23)$$

$$0 = R_r I_{qr} + D \Psi_{qr} - \omega_o \Psi_{dr} \quad (24)$$

$$0 = R_r I_{dr} + D \Psi_{dr} + \omega_o \Psi_{qr} \quad (25)$$

- Stator and rotor flux linkage equations:

$$\Psi_{qs} = L_s I_{qs} + L_m I_{qr} \quad (26)$$

$$\Psi_{ds} = L_s I_{ds} + L_m I_{dr} \quad (27)$$

$$\Psi_{qr} = L_m I_{qs} + L_r I_{qr} \quad (28)$$

$$\Psi_{dr} = L_m I_{ds} + L_r I_{dr} \quad (29)$$

It will be shown in subsequent sections that the above equations are very useful in the motor model representation and in explaining the concept of the DTC.

2.3 d-q Equivalent Circuit

When a DTC drive controls the induction motor, the control computation is almost written in the stationary d-q frame. Since actual stator variables either to be measured or calculated are all in stationary a-b-c frame, frame transformation should be used in control. A simple transformation from stationary a-b-c quantities to stationary d-q quantities is done by using Eqs.(1, 15), which leads to:

$$Y_{qs} = (2/3) \operatorname{Re}[Y_a(t) + a \cdot Y_b(t) + a^2 \cdot Y_c(t)] \quad (30)$$

$$Y_{ds} = -(2/3) \operatorname{Im}[Y_a(t) + a \cdot Y_b(t) + a^2 \cdot Y_c(t)] \quad (31)$$

By using the phasor diagram, Fig. 3, we can rewrite the two previous equations in a simpler form. Note that in our case $\theta_a = 0$ so that:

$$Y_{qs} = Y_a(t) \quad (32)$$

$$Y_{ds} = -(1/\sqrt{3}) [Y_b(t) - Y_c(t)] \quad (33)$$

As any motor is 3-wires three-phase load:

$$Y_a(t) + Y_b(t) + Y_c(t) = 0 \quad (34)$$

Therefore Eq.(33) can be rewritten as:

$$Y_{ds} = -(1/\sqrt{3}) [Y_a(t) + 2 Y_b(t)] \quad (35)$$

This is another benefit of using the stator reference frame that we need to measure only two of three-phase

system variables to complete identification of the d-q model.

2.4 Torque Equations

A simple way to obtain the output torque, also called developed or electromagnetic torque, of a three-phase induction motor is to consider the generated electric power associated with the speed voltage term of Fig. 2 as:

$$P_e = (3/2) \operatorname{Re} [-j\omega_o \Psi_r I_r^*] \quad (36)$$

where I_r^* is the complex conjugates of I_r , this equation can be translated into:

$$P_e = (3/2) \omega_o [\Psi_{qr} I_{dr} - \Psi_{dr} I_{qr}] \quad (37)$$

The relationship between the electrical angular frequency ω_o and the mechanical angular speed ω_m , which represents the actual rotor speed in radians per second, is:

$$\omega_o = p \omega_m \quad (38)$$

where p is the number of machine pole pairs. Also the developed power can be expressed as:

$$P_e = T_e \cdot \omega_m \quad (39)$$

From the previous three equations, the developed electromagnetic torque can be expressed in d-q form as:

$$T_e = (3/2) p [\Psi_{qr} I_{dr} - \Psi_{dr} I_{qr}] \quad (40)$$

By substitution from Eqs.(28, 29) in the previous equation we find that:

$$T_e = (3/2) p [\Psi_{ds} I_{qs} - \Psi_{qs} I_{ds}] \quad (41)$$

The previous equation can be rewritten in space vector form as follow:

$$T_e = (3/2) p \Psi_s \times I_s \quad (42)$$

Other forms of torque equations are applicable. For example, by using Eq.(8) with Eq.(42), we can express the electromagnetic torque in terms of rotor and stator currents as:

$$T_e = (3/2) p L_m I_r \times I_s \quad (43)$$

Also by using Eqs.(8, 9) with Eq.(42), we can express the electromagnetic torque in terms of rotor and stator fluxes:

$$T_e = (3/2) p [L_m / (L_s L_r - L_m^2)] \Psi_r \times \Psi_s \quad (44)$$

The previous equations are very important in the DTC theory explanation and its analysis. Although the torque expressions above are derived from stationary reference frames, they are valid for other reference frames [3].

3. DIRECT TORQUE CONTROL CONCEPT

Generally, the developed torque by any motor is proportional to the cross-product of the stator flux linkage space vector and the rotor flux linkage space vector [4, 5].

$$T_e = k \Psi_r \times \Psi_s \quad (45)$$

where k is constant. And with reference to Fig. 5:

$$T_e = k \Psi_r \Psi_s \sin \delta \quad (46)$$

which is called the torque production equation. Ψ_r is the rotor flux vector's magnitude, Ψ_s is the stator flux vector's magnitude and δ is the angle between them, called the torque angle. By comparing Eq.(46) to (44), the three-phase induction motor torque production equation can be written as:

$$T_e = (3/2) p (L_m / \sigma L_s L_r) \Psi_r \Psi_s \sin \delta \quad (47)$$

where $\sigma = 1 - (L_m^2 / L_s L_r)$; is the leakage coefficient of the motor. It is clear from the torque production equation that the torque can be directly controlled by changing the rotor flux magnitude, stator flux magnitude or the angle between them. In the case of dc motors, they have stationary perpendicular magneto-motive forces. So, the torque angle δ is constant and equal to 90 degrees. The dc motor drives introduced the direct torque control concept, where torque is directly proportional to armature current [4] up to the rated limit. But in the case of three-phase ac motors, the situation is different. The latter has a stator and rotor rotating magnetic fields. The rotor and stator fluxes space vectors rotate along the air gap periphery with an angular speed equal to the three-phase supply angular frequency and with a certain angle δ apart.

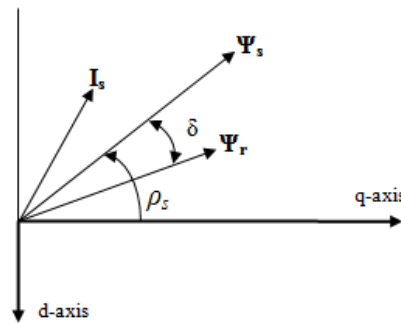


Fig. 5. Rotor and stator flux space vectors

The flux magnitudes are normally kept as constant as possible, and torque is controlled by varying the angle between rotor flux and stator flux vectors [4]. Practically the torque is changed by accelerating or decelerating the stator flux vector relative to the rotor flux vector, which can be assumed to be constant during the control action. Thus a quick change in stator flux angle leads to an instantaneous change in torque value. In the case of synchronous motors, the rotor and stator circuits are separated, the rotor flux can't slip the rotor shaft and since the electrical time constant usually is much smaller than the mechanical time constant, the rotating speed of stator flux, with respect to the rotor flux, can be easily changed [6]. In the case of induction motors and from the previous model, the stator flux space vector is related to the rotor flux space vector by the following formula:

$$D \Psi_r + [(1/\sigma \tau_r) - j\omega_o] \Psi_r = (L_m / \sigma L_s \tau_r) \Psi_s \quad (48)$$

where $\tau_r = L_r / R_r$ is the rotor time constant. This formula can illustrate the nature of rotor flux dynamic response for a step change in stator flux. It can be obtained by substituting from Eqs.(8, 9) into Eq.(7). In the s-domain, the same expression can be written as:

$$\Psi_r = [(L_m / L_s) / (1 + s \sigma \tau_r)] \Psi_s \quad (49)$$

This entails that the rotor flux cannot react quickly to changes in the stator flux, as there is a first-order delay relationship between the two fluxes. Thus the rotor flux vector follows the stator flux vector with a time delay related to the time constant $\sigma \tau_r$ [7]. Hence, the rotor flux changes slowly compared to the stator flux [5]. Thus, rotor flux is relatively stable and can be assumed constant during quick changes in the stator flux. The assumption of constant rotor flux can be justified when the control action is much faster than the rotor electrical time constant multiplied by the motor leakage coefficient. This determines a quick increase in the angle between the two fluxes vectors and, accordingly, in the torque [8].

3.1 Induction Motor DTC principles

The principle of DTC operation is to select stator voltage vectors according to the differences between the reference stator flux and torque and their actual values [5]. The actual instantaneous torque and stator flux linkage values are calculated from stator variables, namely stator voltage and current, using a closed-loop estimator [8]. Optimal stator voltage vectors are selected to limit the flux and torque errors within predetermined bands for flux and torque hysteresis. The required optimum voltage vectors depend on the stator flux space vector position, available switching vectors and the flux of stator needed and torque. The control scheme aims to

keep the flux linkage constant (within a hysteresis band) [5], ensuring that the magnitude of the rotor space flux vector remains constant as well. The torque is thus controlled by varying the relative angle between the stator and the rotor fluxes. Therefore, the induction motor torque control using DTC depends only on the stator flux vector variation without information about the motor (except for stator resistance to calculate the flux linkage) [5]. To control the stator flux variation, the controller selects one of six voltage vectors by a voltage source inverter, as shown.

3.2 Inverter Voltage Space Vectors

The three-phase voltage source inverter in Fig. 6 illustrates the six available voltage vectors used to control the stator flux and torque in a conventional ac motor, where E is the inverter dc link voltage, and S_a , S_b and S_c are the switching functions of the inverter switches. Each switch may be connected to the dc link negative or positive voltage terminals. Meanwhile, these switches are represented by one status and zero status corresponding to the positive and the negative voltage, respectively [9], which reflects on the motor line voltage. When the inverter supplies a symmetrical ac motor with no neutral connection, the stator space voltage vector can be expressed in terms of the dc link voltage E and the inverter gating signals (S_a , S_b , S_c) by the following equation [10]:

$$V_s = (2/3) E [S_a + a S_b + a^2 S_c] \tag{50}$$

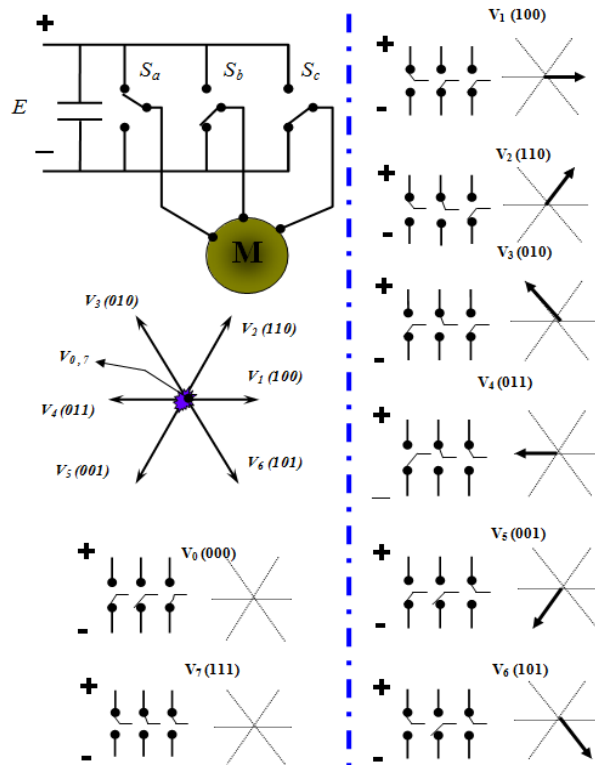


Fig. 6. Available stator space voltage vectors

According to the combination of switching modes, the stator space voltage vectors V_s (S_a , S_b , S_c) are specified in eight distinct vectors. Two of them represent the space zero voltage vectors V_s (1,1,1) and V_s (0,0,0), while the others are nonzero space voltage vectors, e.g. V_s (1,0,0),..., V_s (1,0,1), as shown in Fig. 6 [11, 4]. The space voltage vectors, generated by the inverter and applied to the motor stator winding, control the stator flux linkage space vector movement as shown.

3.3 Stator Flux Movement Control

The stator flux linkage space vector of an induction motor can be expressed in the stationary reference frame by using Eq.(3) as follow:

$$\Psi_s = \int (V_s - R_s I_s) dt \quad (51)$$

During the switching interval Δt , each voltage vector is considered to be constant, and from Eq.(50) the previous equation can be rewritten as:

$$\Psi_s = V_s (S_a, S_b, S_c) \Delta t - \int R_s I_s dt + \Psi_{s0} \quad (52)$$

where Ψ_{s0} is the initial stator flux linkage at the instant of switching. Except at low voltage levels, the stator resistance drop can be neglected. Thus Eq.(52) can be written as:

$$\Delta \Psi_s = V_s (S_a, S_b, S_c) \Delta t \quad (53)$$

where, $\Delta \Psi_s$ is a vector in the same direction as the stator voltage space vector and scaled by the switching interval. This implies that the end of the stator flux vector will move in the direction of the applied voltage vector. As shown in Fig. 7, the vector $\Delta \Psi_s$ or $(V_s \Delta t)$ has two components. The radial component is responsible for flux magnitude control and the tangential one for flux angle control. Also, they are named amplitude and rotation control components [6].

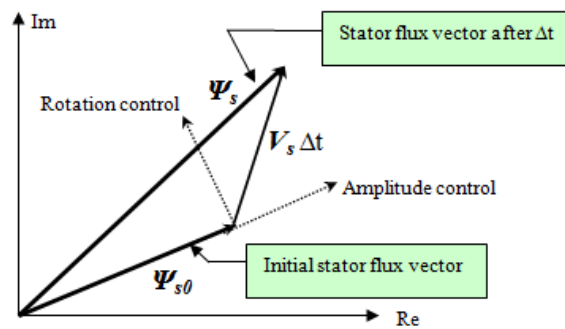


Fig. 7. Stator flux vector radial & tangential movement

4. DTC SCHEME IMPLEMENTATION

A very simple structure characterizes the direct torque control scheme. It mainly consists of two functional blocks [12]:

- Torque and flux estimator (TFE).
- Voltage vector selector (VVS).

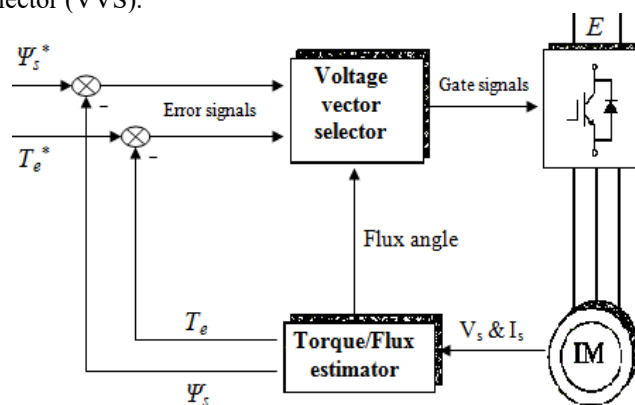


Fig. 8. Basic direct torque control scheme

The core of the DTC scheme is implemented by the basic functional blocks illustrated in Fig. 8 [13].

The torque/flux estimator (TFE) is a very important element in the implementation of the DTC scheme. The DTC scheme needs continuous flux and torque on-line measurements, and there are no sensors that can measure their actual values. The objective of this block is to estimate the actual values of the stator flux linkage space vector (magnitude and angle) referred to the stationary (stator) reference frame and the developed electromagnetic torque level as feedback signals. The dynamic inputs to the torque/flux estimator are the stator voltages and currents.

4.1 Torque/Flux Estimator

To know how the torque/flux estimator calculates its output quantities, we should return to the induction motor mathematical model referred to as the stationary d-q frame and the a-b-c to d-q transformation. Also, let us consider that the analysis of the DTC by digital computers is often done using discrete systems. So, we will define T_s as the sampling interval and k as the sample number, which takes zero or positive integers. The calculation algorithm is as follows:

4.1.1 Calculation of stator direct and quadrature axis voltages:

Two possible methods can be used to calculate the stator terminal voltages of an induction motor in the d-q reference frame fixed to the stator (V_{qs} , V_{ds}). The conventional method is to measure the three-phase motor terminal voltages and transform them to d-q axes voltages [9] by using the transformation equations (32, 35). In this case, two voltage transformers are employed to measure V_{ab} and V_{bc} , which may be a source of error. The second method can be recognized by reviewing equations (50, 15), where the stator voltage space vector and its d-q components are easily calculated from the dc link voltage E and the inverter switches state (S_a , S_b , S_c) at the k^{th} sampling instant as:

$$V_s(k) = (2/3) E [S_a(k) + a S_b(k) + a^2 S_c(k)] \quad (54)$$

$$V_{qs}(k) = \text{Re}[V_s(k)] \quad \& \quad V_{ds}(k) = -\text{Im}[V_s(k)] \quad (55)$$

Thus, no voltage-measuring equipment is needed. At any sampling instant k , the stator voltage space vector is equal to V_0 , $V_1 \dots$ or V_7 . Table 1 shows how we can get the d-q components of each space voltage vector [6], where $V_s = (2/3) E$ is the magnitude of the stator voltage space vector.

Table 1: Values of q - d components for the eight stator voltage space vectors

| | V_0 | V_1 | V_2 | V_3 |
|----------|-------|-------|--------------|--------------|
| V_{qs} | 0 | V_s | $0.5 V_s$ | $-0.5 V_s$ |
| V_{ds} | 0 | 0 | $-0.866 V_s$ | $-0.866 V_s$ |

| | V_4 | V_5 | V_6 | V_7 |
|----------|--------|-------------|-------------|-------|
| V_{qs} | $-V_s$ | $-0.5 V_s$ | $0.5 V_s$ | 0 |
| V_{ds} | 0 | $0.866 V_s$ | $0.866 V_s$ | 0 |

4.1.2 Calculation of stator direct and quadrature axis currents:

Only two current transformers are needed to measure the motor currents of two stator phases (I_a , I_b). From equations (32, 35), d-q axis stator currents can be calculated at the k^{th} sampling instant as follows:

$$I_{qs}(k) = I_a(k) \quad (56)$$

$$I_{ds}(k) = -(1/\sqrt{3}) [I_a(k) + 2 I_b(k)] \quad (57)$$

4.1.3 Calculation of stator direct and quadrature axis fluxes:

From equations (22, 23), the stator flux space vector d-q components can be calculated at the k^{th} sampling instant as follows [6]:

$$\Psi_{qs}(k) = \Psi_{qs}(k-1) + [V_{qs}(k) - R_s I_{qs}(k)] T_s \quad (58)$$

$$\Psi_{ds}(k) = \Psi_{ds}(k-1) + [V_{ds}(k) - R_s I_{ds}(k)] T_s \quad (59)$$

where $(k-1)$ is the previous sample. As mentioned before, the stator resistance voltage drop can be neglected, except at low voltage levels which are accompanied by low speed operation. Thus the two previous equations can be written as:

$$\Psi_{qs}(k) = \Psi_{qs}(k-1) + V_{qs}(k) T_s \quad (60)$$

$$\Psi_{ds}(k) = \Psi_{ds}(k-1) + V_{ds}(k) T_s \quad (61)$$

Then the magnitude and the angle of the stator flux space vector can be calculated as follows:

$$\Psi_s(k) = \sqrt{[\Psi_{qs}^2(k) + \Psi_{ds}^2(k)]} \quad (62)$$

$$\rho_s(k) = \tan^{-1}[-\Psi_{ds}(k)/\Psi_{qs}(k)] \quad (63)$$

4.1.4 Calculation of the motor developed torque:

Finally, the instantaneous electromagnetic torque can be calculated as follows [6]:

$$T_e(k) = (3/2) p [\Psi_{ds}(k) I_{qs}(k) - \Psi_{qs}(k) I_{ds}(k)] \quad (64)$$

4.2 Voltage Vector Selector

The stator voltage space vector selector, or simply voltage vector selector (VVS), is the DTC head. It receives the torque and flux error signals and the stator flux position angle and properly selects the suitable space voltage vector. The VVS is mainly composed of three blocks:

- Hysteresis comparator
- Space sector locator
- Switching table/logic

Fig. 9 illustrates a schematic diagram of the conventional VVS main components. The switching table accepts logic signals only. So, it receives its binary data from the hysteresis comparator and the space sector locator.

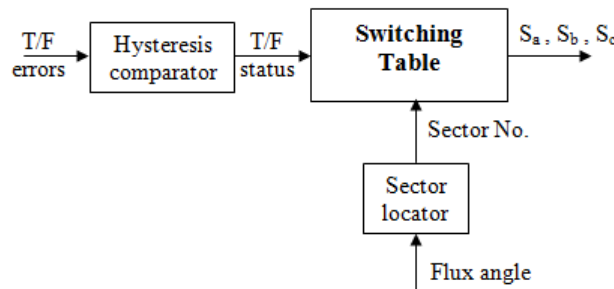


Fig. 9. Schematic diagram of the conventional VVS

4.2.1 Hysteresis Comparator:

The function of the hysteresis comparator is to compare the torque and flux errors with predetermined hysteresis window limits to decide if the torque and flux should be increased or decreased. The output of this block is called torque and flux status. Fig. 10 shows a three-level hysteresis torque error comparator and a two-level hysteresis flux error comparator characteristics [13].

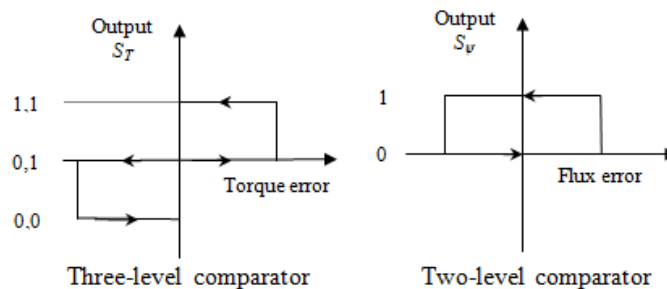


Fig. 10. Torque and flux hysteresis windows

From this figure, it can be seen that the output of the torque error comparator may take the value (0,0), (0,1), or (1,1) depending on the value of the torque error. (0,0) means that torque should be decreased, (1,1) means that torque should be increased. While (0,1) means that torque should be unchanged. Note that (1,0) here is trivial and not used. The output of the flux error comparator may take the value (1) or (0) depending on the value of the flux error. (1) means to increase the flux and (0) means to decrease it. So, the output of the hysteresis comparator is a binary word composed of three bits. This word describes both torque and flux status. The first two bits belong to torque status, and the third bit (the most significant bit) belongs to flux status. Table 2 illustrates binary words corresponding to required torque and flux correction actions.

Table 2: The output binary data of the hysteresis comparator

| | increase Torque | No Action | decrease Torque |
|---------------|-----------------|-----------|-----------------|
| increase flux | (111) | (101) | (100) |
| decrease flux | (011) | (001) | (000) |

Hysteresis windows define the upper and the lower limits to be used to switch between the different torque and flux statuses. Usually, the value of these limits is chosen to be within ± 5 or 2% of the reference value [9]. By nature, the differential hysteresis limits are correlated with the switching frequency of the inverter power solid-state switches. So, the narrower the hysteresis window, the higher the switching frequency will be.

4.2.2 Space Sector Locator:

The function of the space sector locator is to identify the sector on which the stator flux linkage space vector lies at a certain instant. So, its sole input is the flux angle and its output is the flux sector. The space sector locator also expresses the identified sector number as three bits binary word. A three-bit binary word can express eight numbers. Our sector locator uses only six and the remaining two are trivial. Actually, the flux linkage space vector rotates anti-clockwise at synchronous speed. Thus, the flux angle ρ_s varies from 0 to 90 to 180 or -180 to -90 to 0 degrees, and so on.

The scanned 360 degrees are divided into six sectors. Table 3 illustrates these divisions and the corresponding outputs. A possible method to implement the space sector locator is to compare the flux angle to each sector's limits. In Fig. 11, the output of the AND gate will be one if and only if the flux vector lies in sector 1.

Table 3: The output binary data of the sector locator

| | | | |
|-------------|---------------|---------------|--------------|
| Flux angle | (-30 to 30) | (30 to 90) | (90 to 150) |
| Flux sector | S1 | S2 | S3 |
| Output | (001) | (010) | (011) |
| Flux angle | (150 to -150) | (-150 to -90) | (-90 to -30) |
| Flux sector | S4 | S5 | S6 |
| Output | (100) | (101) | (110) |

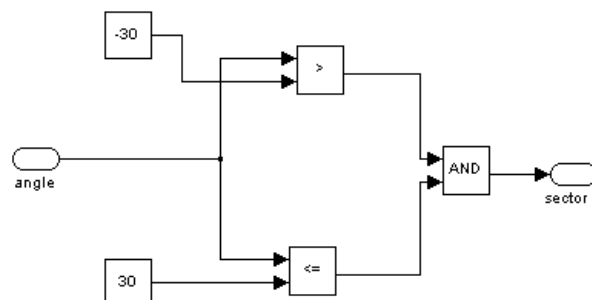


Fig. 11. Elementary space sector identification check

4.2.3 Switching Table/Logic

The switching table or switching logic is the brain of the DTC system. Its function is to select suitable inverter gate signals based on the torque/flux status and the flux vector lying sector. The switching table is simply a two-dimensional look up table. In other words, it can be considered a matrix with 6 rows x 6 columns. Where the hysteresis comparator output determines the row number and the sector locator output determines the column number. Table 4 shows the pre-described switching table [13].

For sure there is a rule to select the nonzero voltage space vector V_1, \dots, V_6 . This rule states that if the stator flux vector is located in sector number (m) in space and the torque status equals (1,1) (i.e. the torque should be increased), there will be two voltage vectors V_{m+1} and V_{m+2} suitable for increasing the torque. The first voltage vector V_{m+1} is used when an increase in the stator flux is also required (i.e. flux status equals 1) but the second voltage vector V_{m+2} is used when a decrease in the stator flux, is required (i.e. flux status equals 0) and so on. Table 4 also summarizes the selection rules of the switching logic [14]. “+1” means one step forward and “-1” means one step backwards from 1 to 6 to 1 as a closed cycle.

Table 4: Optimum switching table & appropriate voltage vector selection rules

| | | | | | | |
|---------|----------------|----------------|----------------|----------------|----------------|----------------|
| | S ₁ | S ₂ | S ₃ | S ₄ | S ₅ | S ₆ |
| Fi & Ti | V ₂ | V ₃ | V ₄ | V ₅ | V ₆ | V ₁ |
| NA | V ₀ | V ₇ | V ₀ | V ₇ | V ₀ | V ₇ |
| Fi & Td | V ₆ | V ₁ | V ₂ | V ₃ | V ₄ | V ₅ |
| Fd & Ti | V ₃ | V ₄ | V ₅ | V ₆ | V ₁ | V ₂ |
| NA | V ₇ | V ₀ | V ₇ | V ₀ | V ₇ | V ₀ |
| Fd & Td | V ₅ | V ₆ | V ₁ | V ₂ | V ₃ | V ₄ |

| | | | |
|----|------------------|----------------------------------|------------------|
| | Ti | NA | Td |
| Fi | V _{m+1} | V ₀ or V ₇ | V _{m-1} |
| Fd | V _{m+2} | V ₀ or V ₇ | V _{m-2} |

F= flux, T=torque, i= increase, d=decrease, NA= no action & S=sector

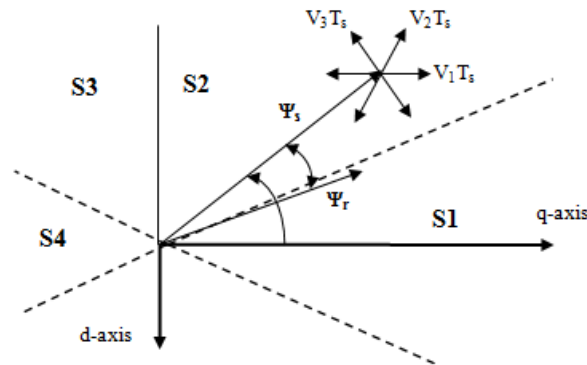


Fig. 12. Voltage vector selection for a flux vector lying in sector 2

Fig. 12 illustrates how the previous rules can apply to a flux vector in sector 2. In case of no action required in torque (torque error is within acceptable limits), a zero voltage vector is selected without consideration of the flux status in order to reduce the torque ripples. To apply a zero voltage vector, V_0 or V_7 can be selected; however, it is found that alternating between them may cause better performance for inverter circuit. This is illustrated in Table 4 too.

5. DTC OPERATION

Referring to Fig. 8, the DTC operation starts with the feedback signals (V_s & I_s), which are fed to the torque/flux estimator (TFE). The TFE calculates the torque and flux magnitude actual values and the flux position angle. Actual flux and torque are compared with the reference values and the errors are fed to the voltage vector selector (VVS).

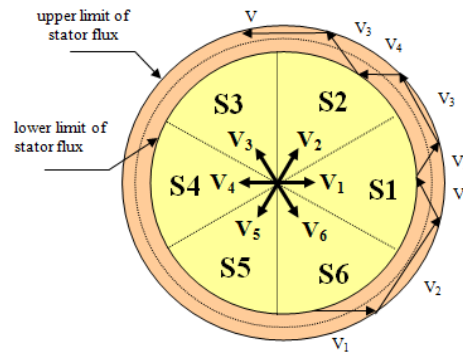


Fig. 13. The stator flux vector tip locus during the DTC operation

The latter receives torque and flux errors and the flux angle. According to error values and angle, the VVS selects the suitable inverter switching state. All of these actions happen outside the motor and are translated inside the motor as a continuous stator flux linkage motion. The latter motion is complex somewhere. It should rotate at a synchronous speed with respect to the stator. Also, it should always be in relative rotation with respect to the rotor flux linkage to increase and decrease the torque angle δ . Finally, its magnitude moves between the lower and upper limits of the flux hysteresis window.

Fig. 13 shows how the appropriate step-by-step voltage vector selections drive the stator flux vector during its motion. In steady state conditions, the stator flux vector draws a circular locus, except for ripples, due to the switching effect [8]. This simple approach achieves a quick torque response. However, undesirable ripples in torque and current accompany the steady state performance [13].

6. SPEED CONTROL BASED ON DTC

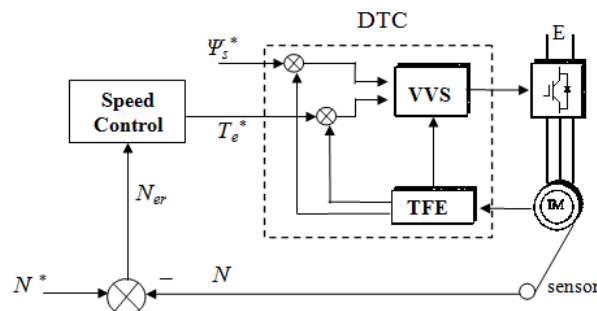


Fig. 14. Speed control based on the DTC scheme

Fig. 14 illustrates the torque control loop (primary loop) and the speed control loop (secondary loop) which is based on DTC. In this system, the speed reference input is compared to the actual speed feedback obtained from a speed sensor. The speed error signal is the input to the speed control block. The resulting output signal from the speed control becomes the torque reference for the DTC subsystem. From here, it is clear that the speed control generates the torque command, i.e., the speed error value determines the torque reference. This leads to the fact that torque control and speed control cannot be achieved at the same time. However, and as mentioned, industrial applications need torque control as well as speed control. In order to swap between torque control and speed control, a torque reference selector is added to the previous system. Fig. 15 illustrates how the torque reference is selected based on the control mode input.

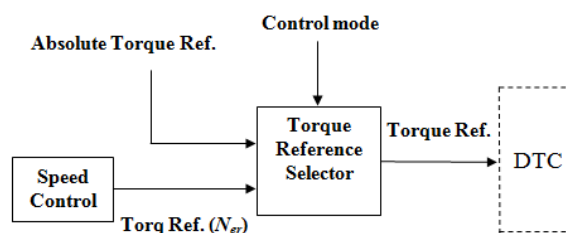


Fig. 15. Torque reference selector schematic diagram

The torque reference selector has three inputs: torque reference as a function of the speed error, absolute torque reference and a control mode. The control mode input can take two values: “low” or “high” (0,1). “0” leads to torque control mode. “1” leads to speed control mode. Only the absolute torque reference is used when the drive works as a torque control. When the drive works as a speed control, only the torque reference, which depends on the speed error, is used. These two references are never used simultaneously [4].

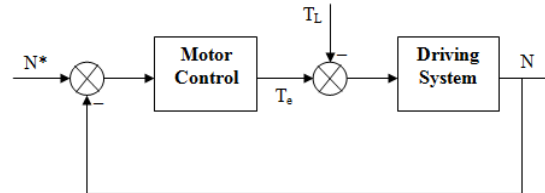


Fig. 16. Block diagram of the motoring system

The output torque reference or demand is processed by the DTC as described before. In fact, the speed control mode also can be divided into two modes of operation: tracking mode and regulating mode. As shown in Fig. 16, the speed reference is the primary input to the system. When the speed reference is changed, the speed controller works to make the motor speed follow the reference speed as possible (tracking). When a load variation occurs (disturbance input), the speed controller resists any probable changes in the motor speed due to this load torque variation (regulating).

7. CONCLUSION

A complete study for three-phase induction motor DTC is presented. A suitable mathematical model choice simplifies the motor's analysis and control. The speed control can be based on the torque control. The switching between torque control and speed control is possible, but both cannot be achieved simultaneously.

ACKNOWLEDGEMENTS

Thanks, ALLAH, for everything. I wish to acknowledge my dear father, Mr. Mohamed Ali Shehata and my beloved teacher Prof. Mohamed Abdel Latif Badr. I ask ALLAH to forgive them and reward them hereafter, Ameen.

REFERENCES

- [1] C. Lascu, I. Boldea, F. Blaabjerg, “A Modified Direct Torque Control for Induction Motor Sensorless Drive,” *IEEE Trans. on Industry Applications*, Vol. 36, No. 1, pp. 122-130, January/ February 2000.
- [2] A. A. Pujol, “Improvements in Direct Torque Control of Induction Motors” Ph.D. Thesis, Catalonia University, Nov. 2000. Internet: <https://www.tesisenred.net/handle/10803/6317>
- [3] Dal Y. Ohm, “Dynamic Model of Induction Motors for Vector Control”, Drivetechnic Inc., Blacksburg, Virginia, 2001. Internet: <http://www.drivetechnic.com/articles/IM98VC1.pdf>
- [4] James N. Nash, “Direct Torque Control, Induction Motor Vector Control without an Encoder” *IEEE Transactions on Industry Applications*, Vol. 33, No. 2, pp. 333-341, March/April.1997.
- [5] David Cheok, Y. Fukuda “A New Torque and Flux Control Method for Switched Reluctance Motor Drives” *IEEE Transactions on Power Electronics*, Vol. 17, No. 4, pp. 543-557, July 2002.
- [6] L. Zhong, M.F. Rahman, W. Y. Hu, K. W. Lim, “Analysis of Direct Torque Control in Permanent Magnet Synchronous Motor Drives” *IEEE Trans. on Power Elec.*, Vol. 12, No. 3, pp. 528-536, May 1997.
- [7] D. Casadei, G. Serra, A. Tani “Performance Analysis of a Speed-Sensorless Induction Motor Drive Based on a Constant-Switching-Frequency DTC Scheme” *IEEE Transactions on Industry Applications*, Vol. 39, No. 2, pp. 476-484, March/April 2003.
- [8] D. Casadei, G. Serra, A. Tani “Implementation of a Direct Torque Control Algorithm for Induction Motors Based on Discrete Space Vector Modulation” *IEEE Transactions on Power Electronics*, Vol. 15, No. 4, pp. 769-777, July 2000.
- [9] S. Osman Madboly, M. Abdel Rahim Badr, H. Farid Soliman “Analysis of the Dynamic Behavior of Direct Torque Controlled Three Phase Induction Motor” M.Sc. Thesis, Ain Shams University, 2004.

-
- [10] Hoang Le-Huy, "Comparison of Field-Oriented Control and Direct Torque Control for Induction Motor Drives" Industry Applications Conference, Thirty-Fourth IAS Annual Meeting, Vol. 2, pp. 1245-1252, Oct. 1999.
 - [11] Yen-Shin Lai, Juo-Chiun Lin, J. J. Wang, "Direct Torque Control Induction Motor Drives with Self-Commissioning Based on Taguchi Methodology" IEEE Trans. on Power Electronics, Vol. 15, No. 6, pp. 1065-1071, Nov. 2000.
 - [12] N. R. Idris, A. Halim Mohamed Yatim, "An Improved Stator Flux Estimation in Steady-State Operation for Direct Torque Control of Induction Machines" IEEE Transaction on Industry Applications, Vol. 38, No. 1, pp. 110-116, Jan./Feb. 2002.
 - [13] D. Casadei, F. Profumo, G. Serra, A. Tani "FOC and DTC: Two Viable Schemes for Induction Motors Torque Control" IEEE Transactions on Power Electronics, Vol. 17, No. 5, pp. 779-786, Sep. 2002.
 - [14] Jun-Koo Kang, Seung-Ki Sul, "New Direct Torque Control for Minimum Torque Ripple and Constant Switching Frequency" IEEE Transactions on Industry Applications, Vol. 35, No. 5, pp. 1076-1082, September/October 1999.

Tech Stocks and Dividend Policy in Malaysia

Ahmad Ibn Ibrahimy¹, and Saad Bin Amjad²

¹Dept. of Economics, Universiti Malaya, Kuala Lumpur, Malaysia

²Dept. of Accounting and Finance, Universiti Malaysia Sarawak, Sarawak, Malaysia

*Corresponding author: dr.ahmad.ibrahimy@um.edu.my

(Received: 8 April 2023; Accepted: 29 April 2023)

Abstract— Malaysia is a developing country, and the capital market is evolving here more than in other emerging markets. Literature on dividend policy has generated extensive theoretical and empirical research, but no broad consensus has emerged after decades of research. The sole determination of this study is to determine the factors affecting the dividend policy of technology stocks listed in Bursa Malaysia. The paper attempts to present the primary studies on dividend policy to provide a thorough understanding of technology corporations' payout practices in Malaysia and reaches inconclusive evidence.

Keywords: Dividend policy, Technological corporation, Malaysia

1. INTRODUCTION

The stock market can be considered a useful foundation for corporations to increase cash. Besides, the stock market provides a channel for technology stocks to expand their business through capital raising and makes the business go public. Several internal and external factors are there that effects dividend policy in Malaysia. Porta et al. (1998) state that several internal factors include economic stability, liquidity, profitability, and investment opportunities. In contrast, technological advancement, market growth, change in consumer taste and legal settings are some external factors. They have a great concern with dividend payments which increase the confidence among shareholders. Dividend policies correlate to other financial and investment decisions (Lahiri and Chakraborty, 2014), especially for technological corporations.

2. REVIEW OF EMPIRICAL LITERATURE

One of the considerable research subjects of technological corporations is dividend policy. Most of the studies attempted to locate “how” corporations pay a dividend that denotes back to the ‘drivers’ of dividend policy. Each element affecting dividend policy is analyzed quantitatively (Banerjee et al., 2007) and qualitatively (Khan et al., 2017; Dhanani, 2005; Lintner, 1956). But the riddle of dividends remains unresolved. Mokaya (2013) examines the measures of the outcome of dividend policy available in the value of the market share in the Kenyan banking industry by using country-wide financial institutions in Kenya. The authors used the main data pattern of hundred shareholders pinched from the target population of forty-seven thousand shareholders of the countrywide financial institution of Kenya. This study examined the operation of the hypothetical model using ANOVA, where multiple regressions measured the statistics to check the technique that explains the association between market share value and dividend payout.

The result indicates a sturdy and effective correspondence between market share value and dividend payout, which is 0.85. It is also obvious that the growth in the price of shares has resulted in a boom in dividend payouts. The majority of respondents indicated that they considered the payment of dividends as a vital element within the value of shares, which means that growth in a dividend payout grounds an increase in stock price. The observation additionally discovered that the private information of dividends disclosed well signal than different sorts of broadcasting, thereby improving the value of the share. Additionally, comparable results were found by Murekefu and Ouma (n.d.), primarily among 41 organizations quoted from the Securities Trade of Nairobi. Over the while of 2002 to 2010, a statistical regression analysis was pinched from the financial statements. The study determined that the connection between dividend payout and the company's performance was strongly effective. In different

phrases, a company's performance additionally represents shareholders' wealth. At a 1% significant level, the relationship was proven to have a strong positive correlation. This shows that dividend is a considerable component in impelling a company's performance while dividend policy corresponds. Moreover, analysis of regression was used in determining the relationship between a company's performance and dividend payout. Primarily based on their research, dividend pay was measured by the usage of the effective dividend received. The company's overall performance was measured through the net earnings after tax which denotes profitability.

In a study by Zakaria *et al.* (2012), it is explained that there is a significant positive relationship between a company's dividend payout and stock price volatility, which led to a correlation of 0.0026 between them. This study analyses the effect of dividend policy on the stock price volatility of Malaysian indexed production and material organization registered at Bursa Malaysia and covers a duration of six years from the year 2004 to the year 2009. It was primarily based on a sample of 77 companies from Bursa Malaysia and utilizing the least square approach. The author determined that the stock prices turn riskier when the dividend payout is more significant. But this study discovered that only 43.43% of the stock price adjustment are explained by the dividend payout ratio.

On the other hand, in line with the study, Hashemijoo (2012) found a significant negative relationship between dividend payout and stock price adjustments. The result indicates a value of -0.382 and it is considered at a 1% significant level. It showed that a reduction within the dividend payout reasons for growth in the stock price volatility. A sample of 84 corporations from 142 consumer product organizations registered under the primary market of Bursa Malaysia was tested for this study and the usage of multiple regression for six years, from 2005 to 2010. Another study by Ilaboya and Aggreh (2013) was conducted primarily based on organizations indexed within the Nigerian stock market. A sample of 26 corporations throughout several sectors was chosen by a simple random sampling method from 2004 to 2011. Researchers used pooled OLS and panel EGLS methods for this study to test the hypotheses.

Moreover, the researchers performed numerous tests consisting of Multicollinearity, Heteroscedasticity, Autocorrelation, and model specification tests using E-views 7.0. The findings showed that dividend payout imposes a poor and insignificant impact on stock price volatility with a poor coefficient of -0.092 and insignificant at 5% and 10%. Subsequently, this indicated that higher payout ratios could signal lesser stock volatility.

3. TRENDS, PERSPECTIVES, AND CHALLENGES

Investors are attracted to technological securities due to their higher growth potential. Dividend policy is crucial for corporations and shareholders (Chauhan *et al.*, 2019). Investors use it as a gauge to see the future performance and stream of income (Kim and Seo, 2014). Dividend policy in Malaysia is at a diverse level. Corporations modify and determine the dividend policy keeping in view the income generated by them (Lintner, 1956). All the sectors pay dividends, even a small quantity (Pandey, 2003). The reason for this low dividend payment is the lower stream of income. It is observed that the plantation sector pays a higher dividend than technological corporations and the service sector, which pays low dividends compared to other industries listed on Bursa Malaysia. In recent years, Malaysia has been logged as Asia's second-largest dividend payout country. From 1973 to 1977, corporations paid dividends of 0.33%, which increased to 3.7% in 1999. In addition, corporations are delisting and merging with other corporations and stopping paying dividends.

Moreover, Zameer *et al.* (2013) stated that distressed firms are experiencing negative income termination to pay dividends. The growth organizations also do not pay dividends due to lower income compared to dividend-payer organizations. Technological corporations, with their massive progress and funding possibilities, will pay their dividend and, at the same time, will generate poor income. Further investment will be made to expand their business as well. Large corporations generally pay higher dividends because they are transparent in their operations and have better earnings ability.

Malaysian government imposed the tax on dividend income and the imposition of tax on cash dividends is an extra burden to the shareholders than the tax on capital gains. Traders choose to earn returns on capital gain instead of dividend income. In line with Al-Malkawi *et al.* (2010), shareholders focus on after-tax returns, increasing the call for dividends. Tax imposition consequently affects the dividend distributions where the management board tends to increase the retained earnings to increase the shareholders' wealth. Given this, the choice of dividends is vital for technological corporations, which affects the dividend policy of the firms listed on Bursa Malaysia and in attaining the imaginative and prescient of Malaysia ended up with high profits in 2020. The capital market is predicted to boom to RM5.8 trillion (US\$1.93 trillion) with an equity marketplace of RM2.4 trillion (US\$800

billion) via 2020 (Security Commission Malaysia, 2013). Under these conditions, dividend choice is a fundamental issue for technology corporations, significantly impacting financing and funding options. Corporations that pay fewer dividends have greater retained earnings. However, a more significant dividend payment results in low retained earnings. Under these conditions, growing corporations meet their financing needs through external funding. Ultimately, dividend policy impacts a firm's capital structure, affecting not only their funding decision but also their cost of capital.

The dividend is considered a primary concern for shareholders and is more likely to increase the value of the firms. But in Malaysia, it is a significant issue that is also being faced by the technology corporations listed on Bursa Malaysia. Besides, firms listed on Bursa Malaysia face severe conditions and are not profitable due to poor performance. Moreover, firms listed on Bursa Malaysia are over-leveraged and bear a high cost of capital. They are paying high-interest expenses and do not have enough funds to meet their financial obligations. Most of the firms fail to pay the debt due to a decrease in their cash flows which results due to dividend payments. In addition, these firms do not have enough funds available to distribute as dividends. Most of the firms listed on Bursa Malaysia are at a loss and earnings per share also decreased. The operating cash flows are also dropping extensively, and firms are not compensating the shareholders properly. Regarding the standard of dividend policy, Malaysia has no precise policies (Sinnadurai et al., 2021). In accumulation to challenging theoretical bearings among dividend coverage, earlier research has stated that dividend decisions might suffer from different factors, including profits, investment opportunities, firm size, lagged dividends and cash flows.

4. CONCLUSION

The impact of various variables on the dividend payout ratio of firms listed in Bursa Malaysia is significantly important in directing the performance of the markets not only for policymakers but also in terms of investors, portfolio managers and researchers. It is observed that the dividend policy of technology corporations in Malaysia does not follow a particular trend. Future research is suggested to expand to countries other else than Malaysia. Evaluation can be done in terms of the outcome attained from altered nations. Furthermore, dividend policy behaviour can be derived after the endurance of the research among different nations. Moreover, there is a difference in sample size among various sectors of countries. A company's decision to pay dividends should not be based solely on the company's liquidity and leverage level. Corporate managers should allow the dividend to be paid and either accumulate liquidity for this persistence or borrow market funds to pay dividends. Borrowing from the market has the added benefit of signalling to the shareholders that the company's strength has not been harmed otherwise the borrowing would not have been feasible.

REFERENCES

- [1] R. L. Porta, F. Lopez-de-Silanes, A. Shleifer, and R. W. Vishny, "Law and Finance," *Journal of Political Economy*, Vol. 106(6), pp. 1113-1155, 1998.
- [2] P. Lahiri, and I. Chakraborty, "Explaining dividend gap between R&D and non-R&D Indian companies in the post-reform period," *Research in International Business and Finance*, Vol. 30, pp. 268-283, 2014.
- [3] S. Banerjee, V. A. Gatchev, and P. A. Spindt, "Stock market liquidity and firm dividend policy," *The Journal of Financial and Quantitative Analysis*, Vol. 42(2), pp. 369-397, 2007.
- [4] N. U. Khan, Q. Ul Ain, S. Jehan, and A. Shah, "Impact of taxation on dividend policy: Evidence from pakistan," *Research in International Business and Finance*, Vol. 42, pp. 365-375, 2017.
- [5] A. Dhanani, "Corporate dividend policy: The views of British financial managers," *Journal of Business Finance & Accounting*, Vol. 32(7-8), pp. 1625-1672, 2005.
- [6] J. Lintner, "Distribution of incomes of corporations among dividends, retained earnings, and taxes," *The American Economic Review*, Vol. 46(2), pp. 97-113, 1956.
- [7] S. O. Mokaya, D. M. Nyang'ara, and L. T. James, "The effect of dividend policy on market share value in the banking industry: The case of National Bank of Kenya," *International Journal of Arts and Commerce*, Vol. 2(2), pp. 91-101, 2013.
- [8] T. M. Murekefu, and, O. P. Ouma, "The relationship between dividend payout and firm performance: A study of listed companies in Kenya," *European Scientific Journal*, Vol. 8(9), pp. 199-215.
- [9] Z. Zakaria, J. Muhammad, and A. H. Zulkifli, "The Impact of dividend policy on the share price volatility: Malaysian construction and material companies," *International Journal of Economics and Management*, Vol. 2(5), PP. 1-8, 2012.

-
- [10] M. Hashemijoo, A. M. Ardekani, and N. Younesi, "The impact of dividend policy on share price volatility in the Malaysian stock market," *Journal of Business Studies Quarterly*, Vol. 4(1), pp. 111-129, 2012.
- [11] O. J. Ilaboya, and M. Aggreh, "Dividend policy and share price volatility," *Journal Asian Development Study*, Vol. 2(2), pp. 109-122, 2013.
- [12] J. Chauhan, M. S. Ansari, M. Taqi, and M. Ajmal, "Dividend policy and its impact on performance of Indian information technology companies," *International Journal of Finance and Accounting*, Vol. 8(1), pp. 36-42, 2019.
- [13] S. Kim, and J. Seo, "A study on dividend determinants for Korea's information technology firms," *Asian Academy of Management Journal of Accounting and Finance*, Vol. 10(2), pp. 1-12, 2014.
- [14] I. M. Pandey, "Corporate dividend policy and behaviour: The Malaysian evidence," *Asian Academy of Management Journal*, Vol. 8(1), pp. 17-32, 2003.
- [15] H. Zameer, S. Rasool, S. Iqbal, and U. Arshad, "Determinants of dividend policy: A case of banking sector in Pakistan," *Middle-East Journal of Scientific Research*, Vol. 18(3), pp. 410-424, 2013.
- [16] H. N. Al-Malkawi, M. Rafferty, and R. Pillai, "Dividend policy: A review of theories and empirical evidence," *International Bulletin of Business Administration*, Vol. 9, pp. 171-200, 2010.
- [17] P. Sinnadurai, R. Subramaniam, and S. Devi, "The influence of government shareholding on dividend policy in Malaysia," *International Journal of Financial Studies*, Vol. 9(3), pp. 1-28, 2021.

Dual–Adaptive Redundancy Minimisation-Based Channel Estimation Method for MIMO OFDM Systems

Ahmad Hasan, S. M. A. Motakabber* and AHM Zahirul Alam

*Dept. of ECE, International Islamic University Malaysia
Kuala Lumpur, Malaysia*

*Corresponding author: amotakabber@iiium.edu.my

(Received: 26 March 2023; Accepted: 26 April 2023)

Abstract— Filtered Orthogonal Frequency Division Multiplexing (FOFDM) is one of the key candidates for harvesting the features that millimetre wave cellular communication is to offer for the 5G and beyond cellular generation. Its chief robust features are increased throughput, efficient spectral utilisation, and interference immunity. Some strict methodologies must be considered to fully utilise these inherent features, especially those allowing guard tones, accurate CSI management and other filter design parameters. This paper proposes a technique to exploit the added redundancies in pilot-based estimators. Here, the authors present an extension idea of an adaptive weight estimator with dual adaptive weights instead of one unique weight factor. We show that these redundancies are insignificant when considering the massive amount of data to be processed and thus can be eliminated to expedite the estimation process efficiently. We implement a weight-based estimator with the necessary accuracy threshold but faster converging to achieve this goal. Simulations follow to demonstrate the advantages of the proposed method.

Keywords: *Millimeter wave, FOFDM, Channel estimation, Massive MIMO, Pilot signals*

1. INTRODUCTION

Filtered OFDM is popular in communication because of its flexibility in cyclic prefix (CP) length, immunity from noise, custom-size sub-bands, etc. [1]. Its backwards compatibility with OFDM means any network structure compatible with OFDM is also compatible [2],[3]. One of the key points in building a MIMO or Massive MIMO network is to determine which type of filtering is to be used. And how it should be implemented, as nowadays it's normal to use some filter bank in modern 5G and 5G plus cellular networks [4]. The need that gave rise to the conception of F-OFDM was the various interference problem caused by the inexistence of any band separation [5],[6]. Because of this operation in separate bandwidth in separate filter banks, networks can take full advantage of unique CP lengths. It allows the network to carry various data payloads for different services within the same subframe [7]. Especially nowadays, when technologies like the IoT, Machine learning are getting popular, this technology can be enabled to achieve the full benefits. For instance, the data for different interconnected IoT devices can be carried out simultaneously if the system uses the F-OFDM structures, not to mention the numerous user data classification described by the 15 and beyond releases by the 3GPP [8]. Using cellular data for IoT devices is commonplace nowadays since today's bandwidth is sufficient to carry small amounts of IoT data with other significant shares of essential cellular data [9]. Owing to this segregated bandwidth allocation, which is fixed considering the operating waveform parameters and the actual traffic scenario, the ability of the transmitter and the receiver to efficiently separate the data traffic from the interference is crucial, especially during the reception. A slight offset in reception can fail to capture whole data blocks. This is one of the moot points of the research that has been integrating the FOFDM into 5G scenarios. These divided subbands are then aggregated at the receiver to complete the transmission process. To enable the network to use dynamic soft parameter setup for the aerial interface considering various traffic loads [3].

The extra padding for the sub-band filters at the beginning of the payload is compensated at the receiver, so it doesn't affect the transmission mode. It can be easily implemented in OFDM systems. Although because of the use of these sub-bands, the length of the guard tones has to be adjusted to allow for the extra padding required for these filters. But since the bands are separated, FOFDM also allows asynchronous inter-band transmissions, which

can be a handy feature in the modern era of cellular communications [10]. So it can be inferred from the above that some significant problems in OFDM are nonadjustable CP and subcarrier spacing length, spectrum localisation, time domain adjustments, etc. On the other hand, and as mentioned before, F-OFDM is backwards compatible, meaning that all the networking terminology and techniques related to OFDM can also be applied to it. Moreover, adding distinctive F-OFDM properties like strong out-of-band rejection and custom sub-band settings are favourable for the new generation cellular structure [11].

In practice, though, some problems limit the proper use of this technology with a 5G cell structure. It requires some additional components and maintenance to reap all of the benefits. For instance, we need a minimally truncated filter with a fixed window [12]. Localising accurately in both the time and frequency domains is impossible as a tradeoff. Usually, frequency domain analysis is applied for filter operation since it's much more straightforward and renders the whole process a little easier.

In most cases, switchback filtering is used in practice so that when the switch is turned off, the system will return to regular OFDM operation. This is useful when reduced power is suddenly required to shed some load. All of these are treated as separate components. It includes subcarrier spacing, Time to initiate (TTI) duration and CP durations. There's a slight difference in the degree of utilisation as the dual links more often utilise near-frequency sub-bands. In addition, the guard tones are often treated as reserved to save some bandwidth.

Since the new cellular structure for the 5th generation facilitates more diverse traffic situations [13], it's intuitive to exploit this characteristic to make the waveform parameters dynamic. However, it means we still can drawback using the legacy OFDM features.

This paper proposes a weight-based channel estimation method based on legacy pilot estimation methods like least squares and minimum mean square error. But we make our estimator adaptive and devoid of redundancies to balance performance and accuracy compared to some recent works [14],[15]. We analyse both uplink and downlink traffic. We use conventional pilot-based methods compared to the trend of using semi-blind or compressed sensing techniques which is a novel approach. The simulations show the difference between a non-adaptive fixed and an adaptive weight-based estimator.

Hence, we can divide the contribution of this paper into three parts-

- ❖ An intuitive algorithm that uses adaptive weight factors to estimate the channel parameters.
- ❖ A method with reduced redundancy that balances complexity and performance.
- ❖ A vital candidate for the 5G plus era, which requires enormous amounts of user data to be processed in a short time.

The rest of the paper is divided into four sections. The following section discusses the methodology of the scheme and the algorithm. It also describes the underlying techniques of our proposed structure. Then it's the results section demonstrating the simulation results of the scheme. The discussion and conclusion section follows discussing the findings and features of our proposal. Lastly, we have the references used for this work.

2. METHODOLOGY

For this work, we assumed a block-fading system with t transmitting antennas and r receiving antennas. In a block fading system, the fading is considered uniform throughout the transmission of each symbol. The inherent characteristic of the F-OFDM system makes it more system specific but also requires dedicated phase and amplitude compensations [16]. Therefore, it considered separate waveform parameters set according to the traffic scenario. As a result, it offsets the high blockage and path loss in the millimetre wave to a certain degree. It also helps the transmitter and the receiver to separate the user data from the interference [17]. This allows the scheme to incorporate a very flexible subframe structure, carrying various service data within the same subframe. Combined with the sub-frame-specific waveform parameters, we can exploit more flexibility than what is offered by the conventional OFDM systems.

To develop our model, we start by calculating the cyclic prefix length. Here we wish to augment the CP length by n_g , so in our system, if the no of subcarriers is n , we will be able to represent each of the transmitted symbols as follows-

$$f(n) = \sum_{l=0}^{L-1} f_l(n - l(n - n_g)) \quad (1)$$

Where, L is the no of OFDM symbols.

Now, if we want a subset from the symbols described in Eq. (1), we can write as-

$$f_l(n) = \sum_{m=0}^{m+M-1} d_{l,m} e^{\frac{2\pi j m n}{n_a}}, \quad n_g \leq n_a \leq n \quad (2)$$

In Eq. (2) $d_{l,m}$ is the parameters from the debut l -mapped OFDM symbols. These are mapped with the subcarriers of m number symbol in the effective subcarrier mapping range. Since before the filtering operation, each sub-band can be regarded as a conventional OFDM symbol [18], then to express symbols in the k^{th} sub-band, we can write-

$$x_k(n) = f_k(n) \otimes j_k(n) \quad k = 1, 2, 3, \dots, K \quad (3)$$

Where $f_k(n)$ is unfiltered and from the i^{th} sub-band; on the other hand, $j_k(n)$ is the impulse signal from that subband's transmission filter. The symbols generated from Eq. (3) expression are then passed through the noisy channel and face attenuation. This effect is shown in the time domain as follows-

$$x(n) = \sum_{k=0}^{K-1} x_k(n) \quad (4)$$

Now applying convolution theory, we can write-

$$r(n) = x(n) \otimes h(n) + z(n) \quad (4a)$$

$$= \sum_{k=0}^{K-1} x_k(n) \otimes h(n) + z(n) \quad (4b)$$

$$= \sum_{k=0}^{K-1} \{f_k(n) \otimes f_k^1(n) \otimes h(n) + z(n)\} \quad (5a)$$

In Eq.(4a), $r(n)$ is the symbol received as the antenna at the receiver after passing through the sub-band filter. The signal subset is one that we get from Eq. (4). Also, $h(n)$ here is the channel impulse, and the AWGN is represented by $z(n)$. The F-OFDM system we're using uses matched filters. So we can assume such a filter $f_k^2(-n)$ at the receiver has a pairing filter at the transmitter, which decouples the signals in each sub-band. We can represent this as-

$$r_k(n) = r(n) \otimes f_k^1(-n) \quad (5b)$$

$$= f_k^1(-n) \otimes \sum_{k=0}^{K-1} f_k(n) \otimes f_k^1(n) \otimes h(n) + f_k^1(-n) \otimes z(n) \quad (6)$$

As mentioned above, $r_k(n)$ here in Eq. (5b) is the received symbol after filtering by the k^{th} sub-band filter. After that, each sub-band goes through an identical process demonstrated by Eq. (6). This filtering scheme differs from

OFDM before any symbol reaches the receiving terminal. The goal of applying dedicated filter blocks is not to lose synchronisation by adding any phase or amplitude offset [19]. It should be mentioned that it's still possible in F-OFDM to have non-ideal synchronisation in the uplink and receive an accurate phase and amplitude representation at the receiver [20]. Still, for this work, we're considering synchronised uplink for simplicity.

2.1 Proposed Algorithm

Here we present now the algorithm for the proposed estimation scheme:

Input: $\bar{x}, \bar{y}, \bar{z}$
Output: \hat{h} for k attempts
Setup: set residual $r_0 = \hat{y}$; $\hat{h} = 0$; $i = s$; $k = 1$; attempt = 1

while \neq (stopping condition)

Step 1: Start; select $f_k = \max(|h \cdot r_{k-1}, i|)$

Step 2: Create test vector- $L_k = \emptyset \cup f_k$

Step 3: Finalise test vector $L = \max(|h_{L_k}|, i)$

Step 4: Residual $r_a = \bar{y} - h_L h_L^* \bar{y}$; Residual $r_b = \bar{y} - h_L h_L^* \bar{y}^*$

Step 5: Check $r_a \sim r_b$; $r_a > r_b \rightarrow$ step 6 else \rightarrow step 2: $\hat{h} = \hat{h} * f_k(\hat{h})$

Step 6: If $\|r\|_2 < \|r_{k-1}\|_2 \rightarrow$ step 7 else \rightarrow step 4: $i = i + 1$

Step 7: Update $L = i \times f$ or $L_k = L$; $r_k = r$; $k = k + 1$

Step 8: $\hat{h} = \frac{h^* L}{r_a^* r_b}$; end loop

Stop

We can see in step 5 that instead of going on with a single weight factor, it opted for two. It makes the scheme more robust to added noise and interference since the next iteration is based on the difference between the weight factors instead of just one. Hence, sudden changes depicted as outliers in the estimation theory are automatically cut out. We'll see in the results section that this aide to also the asynchronous nature of the sub-bands, which eventually fastens the convergence [21]. A schematic approach to the whole process is given below in Fig. 1.

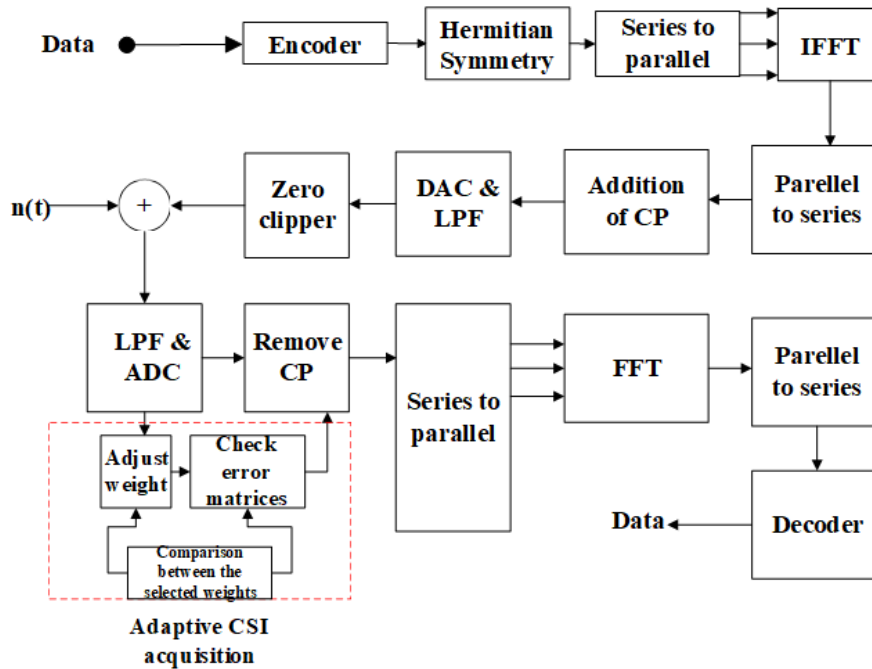


Fig. 1: Schematic diagram for the adaptive CSI acquisition process.

To ease the estimation process, we modelled the channel as a narrowband. It prevents the out-of-bound leakage problem in the OFDM systems [22]. Moreover, robust synchronisation is required in conventional OFDM systems to achieve minimal Inter signal interference (ISI). Here the proposed scheme gets the added immunity thanks to the sub-band division and the intelligent weight selection method. Custom CP length also helps in this regard.

3. RESULTS & DISCUSSION

We used Matlab® for our simulation purposes. For this setup, we simulated 1500 subcarriers. Each subcarrier is considered free of ISI and ICI, i.e. they're deemed ideal. Since we have considered an orthogonal subcarrier, it can also assume zero adjacent channels (ACI) and co-channel interference (CCI). We used the one factor at a time or OFAT method, meaning the number of subcarriers or taps was changed in each simulation. As mentioned at the beginning, the assumption of a block fading scenario allows us to model any impairment caused by the atmosphere as constant for one signal block.

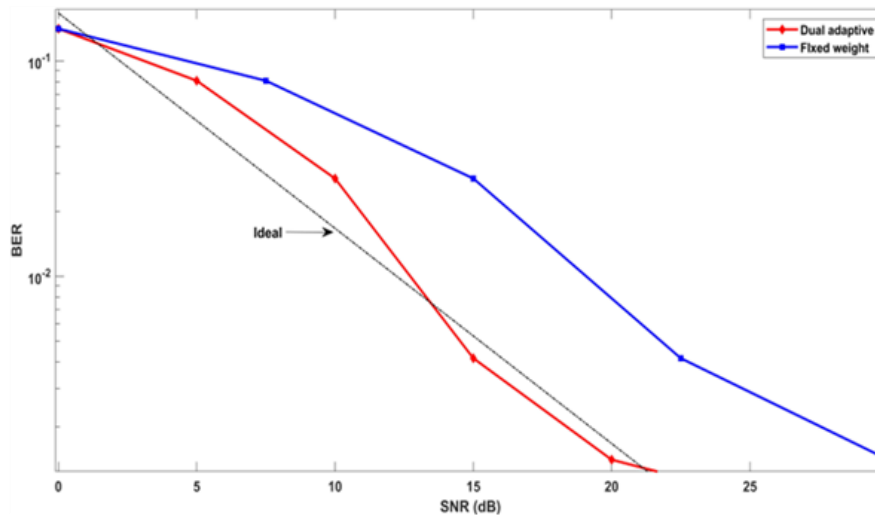


Fig. 2: BER analysis of the proposed method.

Fig. 2 shows that the receiver's response was much more efficient when using two adaptive weights compared to the single fixed weight method. The complexity added is minimal compared to the performance gain, so it is also preferable for the 5G scenario. The better response in the curve can also be characterised as the effect of the reduction of the emphasis on equalisation since, in F-OFDM, it's not essential, unlike OFDM. Fig. 2 shows the improvement in packet error rate, which is also lower than the one mentioned above. It should be noted that this result was obtained by keeping the no of taps up to 8 for the simplicity of the simulations. In other scenarios, it can be further facilitated.

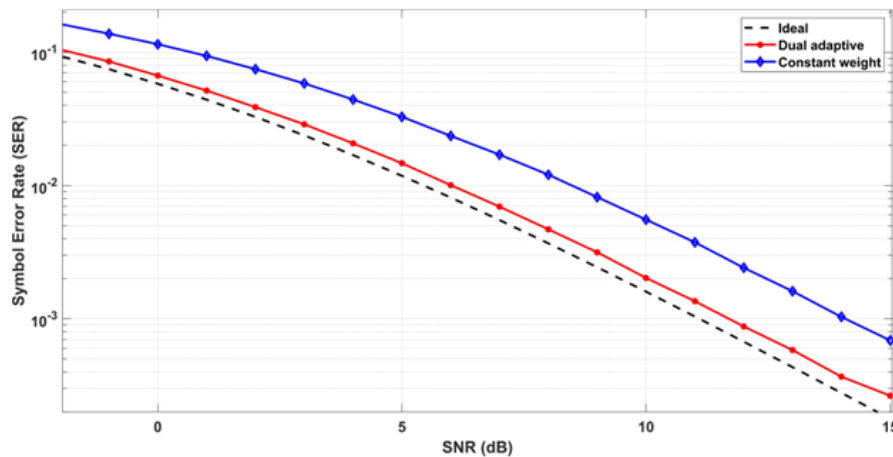


Fig. 3: Symbol error rate (SER) analysis of the estimator.

We also measure the SER analysis of the proposed estimator. It can be inferred from Fig. 3 that the proposed method has a near-ideal response to the question of adjacent symbol contamination. Symbol contamination is severe in modern 5G networks since additional user data has been specified to be sent during transmission per new standards. Therefore, minimising SER can lead to further smooth transmission and faster signal processing.

4. CONCLUSION

In this paper, an intelligent but modest method that exploits the redundancy of the pilot-based estimator was proposed, which adaptively can determine the channel coefficients. In this case, not only single but dual adaptive weight factors have been considered, which further improves the efficiency compared to unique adaptive weight. Simulations show that adaptive weight only needs a slight modification in the algorithm to get promising results. We get the near-ideal response for both BER and SER curves, which can be advantageous for Massive MIMO networks. This work can be judged as an extension of the idea developed by the author in his previous work. Because the terminology and standards are getting increasingly complex in next-gen communication, more straightforward methods with acknowledgeable results are welcomed. Finally, having adaptive weight does add some minor problems like slight to moderate modifications of the receiver, higher uplink traffic etc. However, these are not treated in this work, and the authors would like to leave them as a potential research interest.

REFERENCES

- [1] J. Mao, L. Zhang, P. Xiao and K. Nikitopoulos, "Filtered OFDM: An Insight Into Intrinsic In-Band Interference and Filter Frequency Response Selectivity," in *IEEE Access*, vol. 8, pp. 100670-100683, 2020, doi: 10.1109/ACCESS.2020.2997316.
- [2] L. Zhang, P. Xiao and A. Qudus, "Cyclic Prefix-Based Universal Filtered Multicarrier System and Performance Analysis," in *IEEE Signal Processing Letters*, vol. 23(9), pp. 1197-1201, Sept. 2016, doi: 10.1109/LSP.2016.2590830.
- [3] A. A. Zaidi et al., "A Preliminary Study on Waveform Candidates for 5G Mobile Radio Communications above 6 GHz," *2016 IEEE 83rd Vehicular Technology Conference (VTC Spring)*, 2016, pp. 1-6, doi: 10.1109/VTCSpring.2016.7504096.
- [4] M. Shafi et al., "5G: A Tutorial Overview of Standards, Trials, Challenges, Deployment, and Practice," in *IEEE Journal on Selected Areas in Communications*, vol. 35(6), pp. 1201-1221, June 2017, doi: 10.1109/JSAC.2017.2692307.
- [5] S. K. Sharma, T. E. Bogale, L. B. Le, S. Chatzinotas, X. Wang and B. Ottersten, "Dynamic Spectrum Sharing in 5G Wireless Networks With Full-Duplex Technology: Recent Advances and Research Challenges," in *IEEE Communications Surveys & Tutorials*, vol. 20(1), pp. 674-707, First quarter 2018, doi: 10.1109/COMST.2017.2773628.
- [6] L. Dong et al., "Introduction on IMT-2020 5G Trials in China," in *IEEE Journal on Selected Areas in Communications*, vol. 35(8), pp. 1849-1866, Aug. 2017, doi: 10.1109/JSAC.2017.2710678.
- [7] T. Kebede, Y. Wondie, J. Steinbrunn, H. B. Kassa and K. T. Kornegay, "Multicarrier Waveforms and Multiple Access Strategies in Wireless Networks: Performance, Applications, and Challenges," in *IEEE Access*, vol. 10, pp. 21120-21140, 2022, doi: 10.1109/ACCESS.2022.3151360.
- [8] K. Flynn, "Release 15", 3gpp.org, 2022. Available: <https://www.3gpp.org/release-15>.
- [9] M. Agiwal, A. Roy and N. Saxena, "Next Generation 5G Wireless Networks: A Comprehensive Survey," in *IEEE Communications Surveys & Tutorials*, vol. 18(3), pp. 1617-1655, third quarter 2016, doi: 10.1109/COMST.2016.2532458.
- [10] M. V. Gonzaga Ferreira and F. H. Teles Vieira, "Resource Allocation in f-OFDM Wireless Networks with Delay Estimation Using Service Curve and Envelope Process," *IEEE Lat. Am. Trans.*, vol. 18(7), pp. 1222-1229, Jul. 2020, doi: 10.1109/TLA.2020.9099763.
- [11] P. Guan et al., "5G field trials: OFDM-based waveforms and mixed numerologies," *IEEE J. Sel. Areas Commun.*, vol. 35(6), pp. 1234-1243, Jun. 2017, doi: 10.1109/JSAC.2017.2687718.
- [12] M. V. Gonzaga Ferreira and F. H. Teles Vieira, "Resource Allocation in f-OFDM Wireless Networks with Delay Estimation Using Service Curve and Envelope Process," *IEEE Lat. Am. Trans.*, vol. 18(7), pp. 1222-1229, Jul. 2020, doi: 10.1109/TLA.2020.9099763.
- [13] A. Ghosh, A. Maeder, M. Baker and D. Chandramouli, "5G Evolution: A View on 5G Cellular Technology Beyond 3GPP Release 15," in *IEEE Access*, vol. 7, pp. 127639-127651, 2019, doi: 10.1109/ACCESS.2019.2939938.

-
- [14] K. Mei, J. Liu, X. Zhang, K. Cao, N. Rajatheva and J. Wei, "A Low Complexity Learning-Based Channel Estimation for OFDM Systems With Online Training," in *IEEE Transactions on Communications*, vol. 69(10), pp. 6722-6733, Oct. 2021, doi: 10.1109/TCOMM.2021.3095198.
- [15] F. Han, X. Wang and H. Deng, "A Very-Low Pilot Scheme for mmWave Hybrid Massive MIMO-OFDM Systems," in *IEEE Wireless Communications Letters*, vol. 10(9), pp. 2061-2064, Sept. 2021, doi: 10.1109/LWC.2021.3092073.
- [16] T. Eren and A. Akan, "Channel Estimation for Filtered OFDM Systems in Frequency Selective and High-Speed Multipath Channels," *2018 International Conference on Radar, Antenna, Microwave, Electronics, and Telecommunications (ICRAMET)*, 2018, pp. 32-35, doi: 10.1109/ICRAMET.2018.8683938.
- [17] R. Nissel, S. Schwarz and M. Rupp, "Filter Bank Multicarrier Modulation Schemes for Future Mobile Communications," in *IEEE Journal on Selected Areas in Communications*, vol. 35(8), pp. 1768-1782, Aug. 2017, doi: 10.1109/JSAC.2017.2710022.
- [18] L. Zhang, A. Ijaz, P. Xiao, M. M. Molu and R. Tafazolli, "Filtered OFDM Systems, Algorithms, and Performance Analysis for 5G and Beyond," in *IEEE Transactions on Communications*, vol. 66(3), pp. 1205-1218, March 2018, doi: 10.1109/TCOMM.2017.2771242.
- [19] H. Chen, J. Hua, F. Li, F. Chen and D. Wang, "Interference Analysis in the Asynchronous f-OFDM Systems," in *IEEE Transactions on Communications*, vol. 67(5), pp. 3580-3596, May 2019, doi: 10.1109/TCOMM.2019.2898867.
- [20] H. Chen et al., "Uplink Interference Analysis of F-OFDM Systems Under Non-Ideal Synchronization," in *IEEE Transactions on Vehicular Technology*, vol. 69(12), pp. 15500-15517, Dec. 2020, doi: 10.1109/TVT.2020.3041938.
- [21] L. Zhang, A. Ijaz, P. Xiao, M. M. Molu and R. Tafazolli, "Filtered OFDM Systems, Algorithms, and Performance Analysis for 5G and Beyond," in *IEEE Transactions on Communications*, vol. 66(3), pp. 1205-1218, March 2018, doi: 10.1109/TCOMM.2017.2771242.
- [22] K. S. Chandran and C. K. Ali, "Filtered-OFDM with Index Modulation for Mixed Numerology Transmissions," *2020 6th International Conference on Advanced Computing and Communication Systems (ICACCS)*, 2020, pp. 306-310, doi: 10.1109/ICACCS48705.2020.9074243.
-

Noise Reduction Techniques in ECG Signal

Sakarie M. Muhumed, and Muhammad I. Ibrahimy*

*Dept. of Electrical and Computer Engineering
International Islamic University Malaysia
Kuala Lumpur, Malaysia*

*Corresponding author: ibrahimy@iiu.edu.my

(Received: 2 April 2023; Accepted: 29 April 2023)

Abstract— The problem of noise interference in ECG signals has been addressed in this paper. Specifically, a method has been developed to filter out Electromyography noise (EMG) from ECG signals. A dataset of ECG signals with varying levels of EMG noise has been collected using the MIT-BIH dataset. An algorithm has been designed and implemented using the DA FIR filter coupled with Kaiser windowing technique to filter out the noise. The algorithm has been tested on the collected dataset using MATLAB. The performance of the algorithm has been evaluated by calculating the Signal-to-Noise Ratio (SNR) and the Mean Squared Error (MSE). The effectiveness of the algorithm in reducing the EMG noise in the ECG signals has been demonstrated by the results. The algorithm's limitations and future work were discussed in this paper. Interesting future works could include using other filtering techniques to enhance the performance or deep learning techniques to improve noise cancellation. Overall, the effectiveness of using signal processing techniques to filter out EMG noise from ECG signals has been demonstrated and resulted in clearer and more accurate signals for diagnostic purposes.

Keywords: ECG, EMG, SNR, MSE, DA FIR

1. BACKGROUND

Electrocardiography or ECG, is a collection of records of the heart's electrical activity. Variations in the usual electrical patterns indicate different heart diseases. In their natural state, cardiac cells are electrically polarized. Compared to their outer sides, their interior sides are negatively charged. Depolarization, the primary electrical activity of the heart, can cause these cardiac cells to lose their typical negativity. A wave of depolarization can be carried across the entire heart because of the depolarization spreading from cell to cell. Keeping the electrodes on the body's surface allows one to measure the electric current produced by this wave of depolarization. After the depolarization is finished, a process known as re-polarization allows the cardiac cells to return to their usual polarity. The electrodes can also detect this [1].

1.1 Characteristics of ECG signals

The ECG recorder captures the electrical activity of the heart, represented by each heartbeat as a series of electrical waves with peaks and troughs. Any ECG offers two distinct forms of information. Whether the electrical activity is regular, sluggish, or irregular depends on how long the electrical wave passes the heart. A typical ECG signal (Fig. 1) has a dynamic range of 1 to 10 mV and a frequency ranging from 0.05 to 100 Hz. The five peaks and valleys that make up the ECG signal are denoted by the letters P, Q, R, S, and T. We also occasionally use a mountain named U.

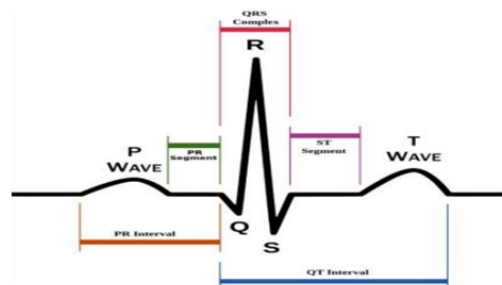


Fig. 1: Typical ECG wave [1]

1.2 Types of noises and artefacts in ECG signals

Continuous noises: This noise is connected to signals from every lead that have identical temporal distributions but different intensities. These noises dominate multiple frequency bands. Electromyography noise is the lower component, power line interference is the medium component, and baseline wanders the higher component when we are talking frequency-wise [2]. Baseline Wander (BW) noise: The baseline wander can be brought on by changes in the impedance of the electrodes and patient movements. Power line interference noise: Background noise in ECGs and other physiological data received from the body surface is frequently caused by power line interference. Electromyography (EMG) noise: All muscles except the heart contract, which is what produces the EMG noise. Transient noise: Since it only lasts for a short duration, white Gaussian noise is the most widespread sort of transitory noise. Its spectral density is uniformly distributed since its immediate value has a Gaussian distribution and power. This noise includes instrument noise, motion artefacts from patient electrodes, and other sorts of noise. But it is impossible to divide this noise into frequency categories [2]. Patient electrode motion artefact: When the electrode equilibrium potential changes, electrode motion artefacts arise. Instrumentation noise: The electrodes, wires, amplifiers, and converters found in all pieces of equipment are the primary sources of instrumentation noise.

2. TECHNIQUES FOR ECG NOISE REMOVAL

When an ECG signal is acquired from the patient, it is usually denoised before doctors can interpret it. As shown in Fig.2, it can only go through the denoising model after adding the noise.

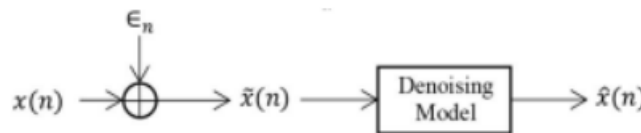


Fig. 2: A typical cardiac cycle's denoising mechanism [3].

2.1 Models for ECG signal denoising based on EMD

Each signal is separated into a few numbers of its intrinsic mode functions using an adaptive repetitive approach named Empirical Mode Decomposition (EMD). Using this repetitive signal breakdown, this empirical mode decomposition separates the entire signal into ordered components, moving from higher frequencies to lower frequencies at each intrinsic mode function level [4]. The EMD procedure's decomposition is based on the signal's local time characteristics; hence it works with nonlinear and non-stationary processes (Fig. 3) [5]. Unlike data analysis techniques like the Fourier transforms, EMD is fully data-driven and does not require any prior knowledge [6].

1. Input: noisy ECG signal $\tilde{x}(n)$
 2. Sifting process
 3. Repetitive application of the sifting process on proto IMF $h_k(n)$ until the stopping criterion (SD) gives the first IMF $c_1(n)$
 4. Residue: $r_1(n) = \tilde{x}(n) - c_1(n)$
 5. $r_1(n)$ might contain some useful signal information, hence the algorithm is run with $r_1(n)$ in place of $\tilde{x}(n)$
 6. Hence, $\tilde{x}(n) = \sum_{i=1}^L c_i(n) + r_L(n)$
 $\tilde{x}(n)$ has L IMFs and the algorithm terminates at the L^{th} iteration, where the residue is either a constant, a monotonic slope, or a function with only one extremum
 7. Thresholding or filtering or adaptive selection of IMFs ($\{c_i(n)\}$) for the purpose of signal reconstruction to get the denoised signal $\hat{x}(n)$
- $$\hat{x}(n) = \sum_{i=1}^L \hat{c}_i(n) + r_L(n)$$
- where $\hat{c}_i(n)$ is filtered IMF
8. Output: $\hat{x}(n)$: denoised ECG signal

Fig. 3: Algorithm 1: EMD-based denoiser's denoising algorithm [7].

Blanco-Velasco et al. concluded after analyzing both clean and noisy ECGs using EMD, using the EMD domain's temporal processing. Since noise and the QRS complex share a similar spectral signature in the high-frequency band, it is difficult to remove the noisy signal while keeping the QRS complex [6]. Lower intrinsic mode functions would have been lost, leading to 11 significant QRS complex distortions. The denoising technique invented to tackle the noisy ECG is described in Algorithm 2 (Fig. 4a), and because of applying this filter, we can see that EEMD can be an effective model to filter out the BW noise, as shown in Fig. 4b.

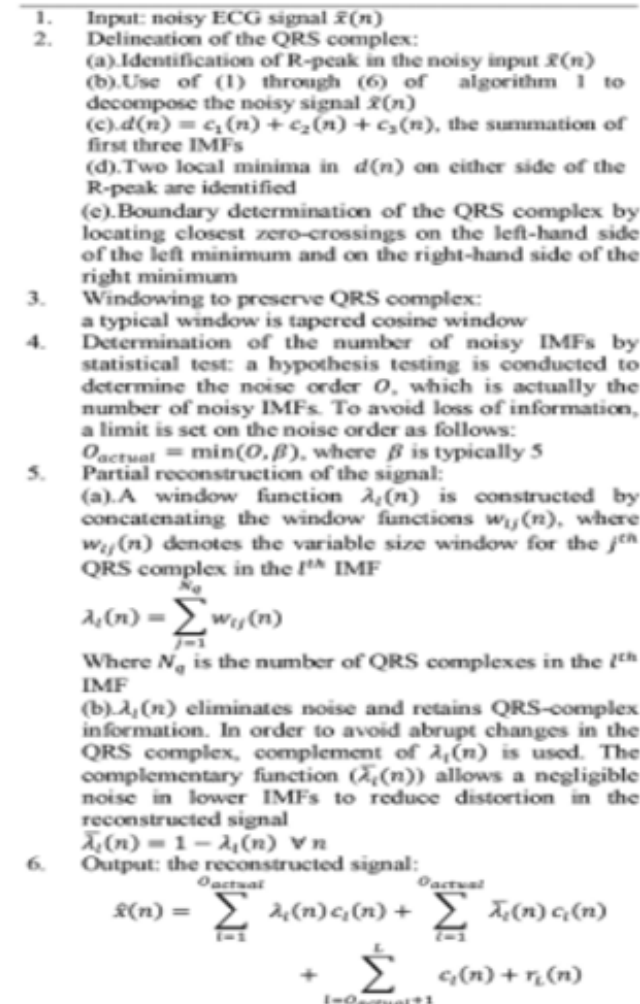


Fig. 4a: Algorithm 2: EEMD-based denoiser's denoising algorithm [3].

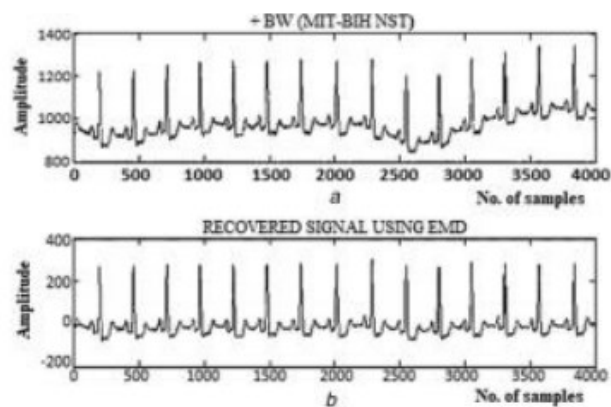


Fig. 4b: ECG signal using EEMD to denoise [3].

2.2 Models for ECG signal denoising based on Wavelet

The time and frequency range of the signal is widened by a WT when seen via the lens of a localized wavelet function. Wavelet transform can offer good time and resolution of frequency at HF and LF. Consequently, a wavelet transform is an excellent option for processing ECG information. The mother wavelet function's contractions, expansions, and translations are used to decompose a signal into a series of fundamental processes, as shown in Fig. 5 [3]. Dyadic WT (DWT) is a great option for analyzing and filtering ECG signals due to its quick computation and multiresolution capability, as shown in Fig. 6 [8].

- | | |
|----|--|
| 1. | Input: $\tilde{x}(n)$ s.t. $\tilde{x}(n) = x(n) + \epsilon_n$, where $\{\epsilon_n\}$ is some noise process with variance σ^2 , where n is the index of $\tilde{x}(n)$ |
| 2. | $d_i(k)$ and $a_L(k)$, detail coefficients and approximate coefficients, are obtained. The coefficients are collectively denoted as $w(k)$ |
| 3. | Shrinking is performed by thresholding to convert $w(k)$ to $w^*(k)$ |
| 4. | Finally, the inverse wavelet transform is taken on $w^*(k)$ to estimate the signal $x(n)$ in the noisy environment, using the filter bank architecture |
| 5. | Output: $\hat{x}(n)$ |

Fig. 5: Algorithm 3: Algorithm followed by the wavelet denoiser [3], [8].

While considering the conventional thresholding methods, researchers have developed various thresholding algorithms and techniques to denoise ECG data. One of these researchers is Smith *et al.*, who discovered the polynomial coefficients [9] utilizing polynomial threshold operators, with least-squares minimization used for optimization. Alfaouri and Daqrouq have offered another denoising method for ECG data. The difference between the noisy and original detail coefficients sets the threshold for a five-level wavelet transformation using Daubechies as the mother wavelet[10].

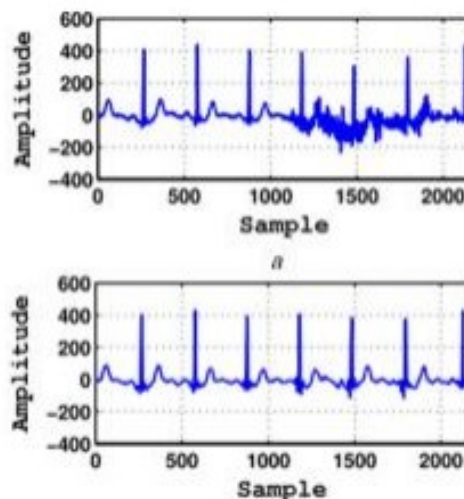


Fig 6: DWT-based ECG denoising (Sym5) [3].

2.3 Models for ECG signal denoising based on Bayesian filter

This category of denoising researches several model-based techniques for denoising ECG signals. Model-based approaches operate under the premise that hidden model states can be estimated using estimation theory. Through a series of measurements, these hidden states are seen. The Kalman filter is one such approach (KF). Although most systems are nonlinear, the fundamental KF assumes a linear model for the system dynamics and observation equations. The original Kalman filter has been improved into other forms, including EKF, EKS, and UKF.

Overviews of the enhanced versions of the standard KF and how they work are provided by Sameni *et al.*, as shown in Fig. 7 [11].

1. Input: x, y, z : the state variables
2. Conversion of the non-linear dynamic ECG model from Cartesian to polar
3. Linearization of the modified model
4. Observation of s_k and ϕ_k , where $\{s_k\}$ are the noisy ECG observations and $\{\phi_k\}$ are the phase observations
5. Prediction of model parameters prior to the implementation of the filter

Fig. 7: Algorithm 4: Bayesian-filter-based denoising algorithm [11].

A marginalized particle Extended Kalman filter that addresses the drawbacks of both extended Kalman filter and particle filters has been proposed by Hesar and Mohebbi [12]. This makes use of a brand-new marginalized particle filter and EKF combo. The state model is initially changed by including angular velocity as an AR state, leading to the "marginalized particle extended Kalman filter" (MP-EKF) algorithm, which is used to convert two-state polar EDM into three-state polar EDM. ECG parameters are extracted using techniques like those in [11]. When the signal is first observed, the R-peaks of the ECG cycles are thought to be at position $\theta=0$. Between two consecutive R-peaks, the ECG data's phase ranges from 0 to 2π (or $-\pi$ to π). The distance between the particles and the noisy readings and ECGsynth is evaluated and weighted at each time step in a particle weighting technique. A synthetic ECG 15 signal called ECGsynth is created utilizing the feature parameters that were taken from ECG(θ). Fig. 8 shows the closeness evaluation metric is the Mahalanobis distance, a statistical distance metric. For each particle, this weighting method is applied in each time step.

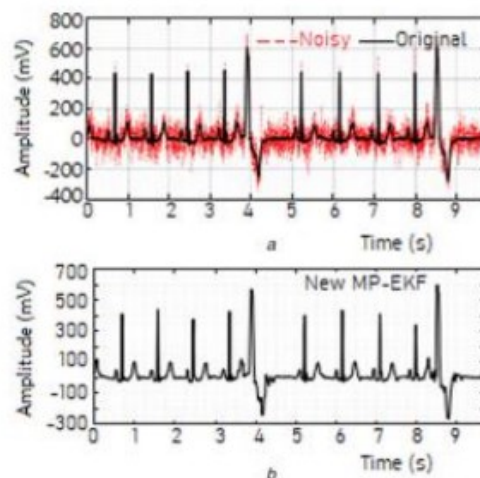


Fig. 8: Using the new MP-EKF for ECG denoising [13].

3. METHODOLOGY

The paper aims to design and implement an algorithm to filter out or remove the persistent EMG noise from the acquired ECG signal for correct reading and interpretation by doctors.

3.1 Resources and Materials.

FIR filter: Because of the strong design techniques available for them, as well as their inherent stability, FIR filters are commonly employed. The ease with which linear phase can be achieved when implemented in non-recursive form. Several methods exist for creating an FIR low pass filter, including the equiripple filter, the least square approach, and the windowing method. The Kaiser, Rectangular, Hamming, Hanning, and Blackman functions are designed using the windowing method. The main features for creating a filter include a cut-off frequency of 100Hz and a sampling frequency of 360Hz (based on the MIT/BIH database). In FIR window filters,

the cut-off frequency at the 3 dB point is approximately 91.8333 Hz. The window length for rectangular, Hanning, and Hamming is 18 and 16, respectively. For Bartlett and Blackman, the filter order is 37 and 19, respectively. The Kaiser window has a filter length of 14 with a phase delay of 0.1047 rad/Hz and a cut-off frequency at 3dB of 89.60449Hz. MATLAB: A strong, complete, and user-friendly platform for technical computations in MATLAB. One of its significant advantages is the ability to create one's own reusable tools with MATLAB. The ECG database extraction process takes place in Matlab and is stored at www.physiobank.org. The workspace of Matlab can be used to call the stored ECG signal in the Simulink model. Real-time EMG noise is imported into the workspace and combined with pure ECG in Simulink model after 22 being retrieved from the MIT-BIH noise stress database as an a.mat file. Utilized in the design of the FIR low pass filter is FDATool from Matlab. Various FIR digital filter types are used to cut out high-frequency EMG noise. MIT-BIH: In this study, the data used was sourced from the MIT-BIH Arrhythmia Database on Physio Bank. The recordings were digitized at a high frequency and stored in a specific format, including a header file with patient information, a binary file containing the ECG signal, and a binary file with annotations. Additionally, half of the database was made available for free use. The EMG data used was taken from the MIT-BIH Noise Stress Database, also found on Physio bank, which includes recordings of both ECG and noise specific to ambulatory settings. These recordings were collected from physically active volunteers and recorded using standard equipment. Distributed Arithmetic (DA) FIR filter: Digital FIR filters can be efficiently implemented in FPGA structures using distributed arithmetic. The DA approach is frequently utilized to calculate sums of products with constant coefficients. In this scenario, the partial product term is multiplied by a constant (i.e., scaling). The Look-up Table (LUT), Shift Registers, and Scaling Accumulator components of the DA method replace the general-purpose multipliers and considerably improve the performance of the implemented filter. These blocks must be effectively mapped onto the logic cells of an FPGA. Compared to current designs for FIR Filters, the suggested architecture offers an effective area-time-power implementation that entails much-reduced latency and area-delay complexity. The equations for the DA FIR filter for calculating SNR and MSE are as follows:

$$SNR = 10 \log_{10} \frac{\sum_{i=0}^N (ECG_{raw})^2}{\sum_{i=0}^N (ECG_{raw} - ECG_{filtered})^2}$$

$$MSE = 10 \log_{10} \frac{\sum_{i=0}^N (ECG_{raw} - ECG_{filtered})^2}{N}$$

4. CONCLUSION

This literature review aimed to evaluate the effectiveness of various ECG denoising methods in medical applications. Three key aspects of ECG denoising were investigated to support patient diagnosis and treatment: noise acquisition, eradication of prevailing noises, and contrasting the methods in use today. The results showed that the modified polar extended Kalman filter outperformed conventional denoising approaches for MA, while GAN1 was found to be effective in removing BW and EM noise. Additionally, EWT was determined to be the most appropriate method for removing PLI noise, but promising results were also obtained for CN reduction using DWT (Sym6) and MABWT (Soft).

The paper involves designing an algorithm to remove high-frequency EMG noise from ECG signals. The methodology is clearly defined, and the process includes designing and testing the algorithm on a corrupted ECG signal in MATLAB to produce a filtered pure ECG signal. The effectiveness of the designed algorithm in removing EMG noise from the ECG signal will be analyzed and discussed based on the results obtained. Overall, the study provides valuable insights into ECG denoising techniques and highlights the importance of selecting appropriate methods to ensure accurate diagnosis and treatment in medical applications.

REFERENCES

- [1] C. Saritha, V. Sukanya, and Y. N. Murthy, "ECG Signal Analysis Using Wavelet Transforms," 2008.
- [2] F. Liu, Y. Xu, and Y. Yao, "Highly Efficient Low Noise Solutions in ECG Signals," in *Journal of Physics: Conference Series*, IOP Publishing Ltd, Apr. 2022. doi: 10.1088/1742-6596/2246/1/012030.
- [3] S. Chatterjee, R. S. Thakur, R. N. Yadav, L. Gupta, and D. K. Raghuvanshi, "Review of noise removal techniques in ECG signals," *IET Signal Processing*, vol. 14, no. 9. Institution of Engineering and Technology, pp. 569–590, Dec. 01, 2020. doi: 10.1049/iet-spr.2020.0104.

-
- [4] K. M. Chang, "Arrhythmia ECG noise reduction by ensemble empirical mode decomposition," *Sensors*, vol. 10, no. 6, pp. 6063–6080, Jun. 2010, doi: 10.3390/s100606063.
 - [5] A. Boudraa, J. Cexus, and E. Navale, "DENOISING VIA EMPIRICAL MODE DECOMPOSITION."
 - [6] M. Blanco-Velasco, B. Weng, and K. E. Barner, "ECG signal denoising and baseline wander correction based on the empirical mode decomposition," *Comput Biol Med*, vol. 38, no. 1, pp. 1–13, Jan. 2008, doi: 10.1016/j.compbiomed.2007.06.003.
 - [7] N. E. Huang *et al.*, "The empirical mode decomposition and the Hubert spectrum for nonlinear and non-stationary time series analysis," *Proceedings of the Royal Society A: Mathematical, Physical and Engineering Sciences*, vol. 454, no. 1971, pp. 903–995, 1998, doi: 10.1098/rspa.1998.0193.
 - [8] B. Chen, Y. Li, and N. Zeng, "Centralized Wavelet Multiresolution for Exact Translation Invariant Processing of ECG Signals," *IEEE Access*, vol. 7, pp. 42322–42330, 2019, doi: 10.1109/ACCESS.2019.2907249.
 - [9] C. B. Smith, S. Agaian, and D. Akopian, "A wavelet-denoising approach using polynomial threshold operators," *IEEE Signal Process Lett*, vol. 15, pp. 906–909, 2008, doi: 10.1109/LSP.2008.2001815.
 - [10] M. Alfaouri and K. Daqrouq, "ECG Signal Denoising By Wavelet Transform Thresholding," *Am J Appl Sci*, vol. 5, no. 3, pp. 276–281, 2008.
 - [11] R. Sameni, M. B. Shamsollahi, C. Jutten, and G. D. Clifford, "A nonlinear Bayesian filtering framework for ECG denoising," *IEEE Trans Biomed Eng*, vol. 54, no. 12, pp. 2172–2185, Dec. 2007, doi: 10.1109/TBME.2007.897817.
 - [12] H. D. Hesar and M. Mohebbi, "An adaptive particle weighting strategy for ECG denoising using marginalized particle extended kalman filter: An evaluation in arrhythmia contexts," *IEEE J Biomed Health Inform*, vol. 21, no. 6, pp. 1581–1592, Nov. 2017, doi: 10.1109/JBHI.2017.2706298.
 - [13] H. D. Hesar and M. Mohebbi, "ECG Denoising Using Marginalized Particle Extended Kalman Filter with an Automatic Particle Weighting Strategy," *IEEE J Biomed Health Inform*, vol. 21, no. 3, pp. 635–644, May 2017, doi: 10.1109/JBHI.2016.2582340.
-

Effect of Inductor for Designing an Inverter to Maximize Solar Panel Power Output

Muhammad Wasif Hasan and AHM Zahirul Alam

*Department of Electrical and Computer Engineering, Faculty of Engineering,
International Islamic University Malaysia,
Kuala Lumpur, Malaysia*

*Corresponding author: wasifhasan12@gmail.com

(Received: 2 April 2023; Accepted: 30 April 2023)

Abstract— The current methods to maximize solar cell efficiency have proven too complex for low-power solar applications. In addition, traditional methods, such as changing the orientation of a solar panel, can be too difficult for large photovoltaic arrays. Therefore, in this work, various analyses will be done with the critical components of a solar PV circuit to estimate its maximum power point (MPP). The effect of inductance for designing a solar cell system for maximized power by controlling the DC/DC Boost controller.

Keywords: *Maximum Power Point Tracking, Internet of Things, PV*

1. INTRODUCTION

The sun is a core facet of all living beings as it influences the weather and seasons and makes plant life possible due to its photo-chemical energy being used in photosynthesis. Since fossil fuels are slowly being depleted, the world has transitioned to an all-sustainable future, where solar and wind energy are two of the rising contenders as they are the most abundant. An integral part of a solar cell is converting solar energy to electrical using photovoltaic modules. As solar photovoltaic (PV) panels are more available to consumers, this form of energy harnessing is becoming more widely known. Different techniques are employed to find the maximum power point to maximize the efficiency of these panels.

Using a Maximum Power Point Tracking (MPPT) algorithm is one approach to have a solar panel operate at its maximum power point. Most of the different types of MPPT algorithms probe the entire operating range of the panel to detect where the maximum power is being generated - some examples of integrated circuits which can do so are the LT8490 and the LTC4015[1-2]. The advantage of using this algorithm is that it can find and contrast between a local power peak from a global power maximum. It achieves this by continually sweeping the output range of the panel and detecting the operating conditions where maximum power was reached. After this is done, the system constraints the panel to return to this power point. While these periodic sweeps are being done, the MPPT algorithm will continuously dither the operating point to ensure it stays at/ near the peak [3]. Dithering adds noise to a signal to make quantization distortion less visible.

As global energy demand continues to grow, non-renewable energy sources such as oil are being depleted at an alarming rate. Solar energy is one of the most available forms of energy as it is readily present during the day. Still, the orientation of the solar panels might have to be changed for them to face the sunlight directly. For large PV arrays, this can prove to be an issue as these large panels can be quite cumbersome to move unless they use an automated system.

In this paper, the effect of inductance is observed for designing an inverter and its impact on power tracking.

2. MODELLING OF THE PROPOSED CIRCUIT

A closed loop system will be used with a fixed voltage to monitor the system. The algorithm specified before was the Perturb and Observe method, where the change of the duty cycle is directly proportional to the output voltage change. The system block diagram is shown in Figure 1, along with the main components.

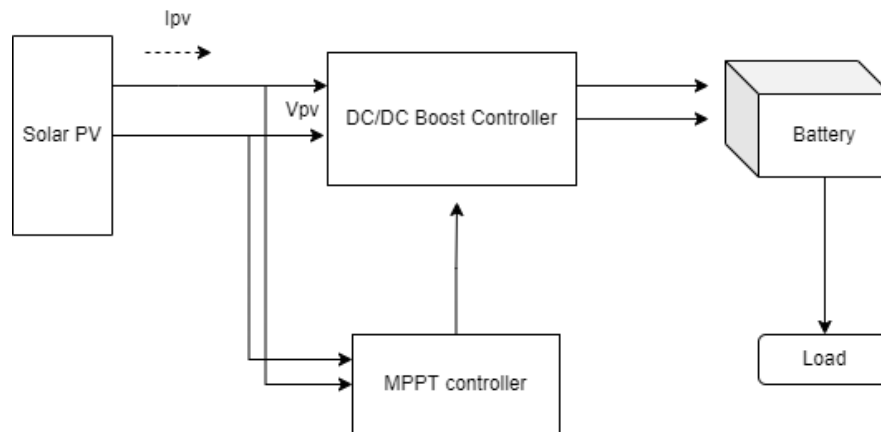


Fig. 1. Block diagram of the proposed system

The circuit is mainly comprised of a Booster circuit, an MPPT Controller and a battery. For the algorithm, the Perturb and Observe method (P&O) can be used to implement the MPPT for solar PV. Several papers have outlined that this algorithm is quite efficient and selects the future value of the output voltage while remembering the current and the past values as it fluctuates [4].

3. THE PROPOSED MAXIMUM POWER POINT TRACKING SYSTEM

This section will focus on the critical circuits that are to be used, and their respective simulations are also shown here for clarity. Formulas for the components are shown where applicable, and detailed calculations are given in the appendix.

The schematic of the Boost circuit is shown below, and the calculations for the inductor and capacitor are elaborated here as well. For this initial analysis, the value of the inductor is increased from 2.5 uH to 22.5 uH with increments of 5 uH.

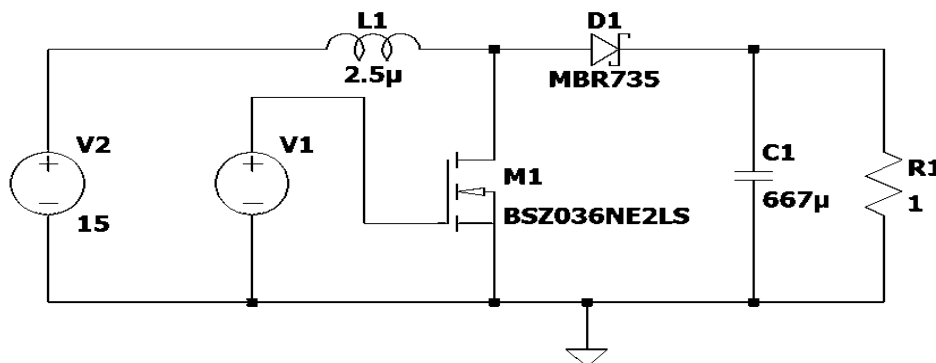


Fig. 2. Schematic diagram of the Booster circuit

The optimum value of the inductor and capacitor are calculated based on eqns. 1 and 2, respectively.

$$L = \frac{R \cdot D(1-D)^2}{2 \cdot F_s} \quad (1)$$

Where, L – inductor value, H, D – duty cycle, F_s – switching frequency, Hz and R – equivalent load, Ω

Calculations for a capacitor:

$$C \geq \frac{V_o \cdot D}{F_s \cdot \Delta V_o \cdot R} \quad (2)$$

Where, V_o – output voltage, V, D – duty cycle, F_s – switching frequency, Hz, ΔV_o – ripple voltage and R – equivalent load, Ω

The schematic of a dual 555 timer is shown in Fig. 3 for controlling the inverter clock.

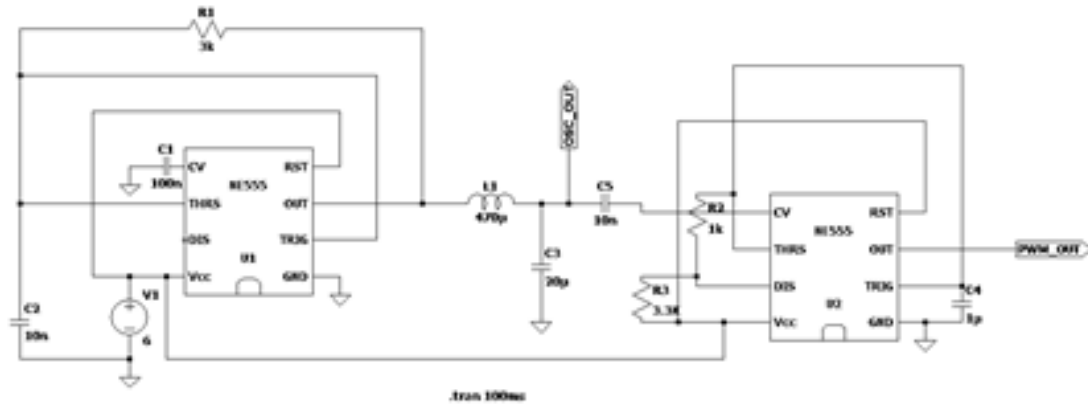


Fig. 3. Schematic of a dual 555 timer

To find the capabilities of an IC with Maximum Power Point Control, LTC3105 is being used.

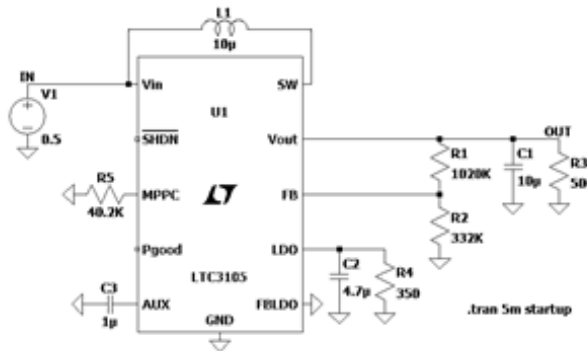


Fig. 4. Schematic of LTC 3105 (DC/DC step-up converter with Maximum Power Point Control)

4. RESULTS ANALYSIS

The simulations for the circuits shown in the previous section are given here. The analysis is done using LTSpice Simulation results for Boost converter:

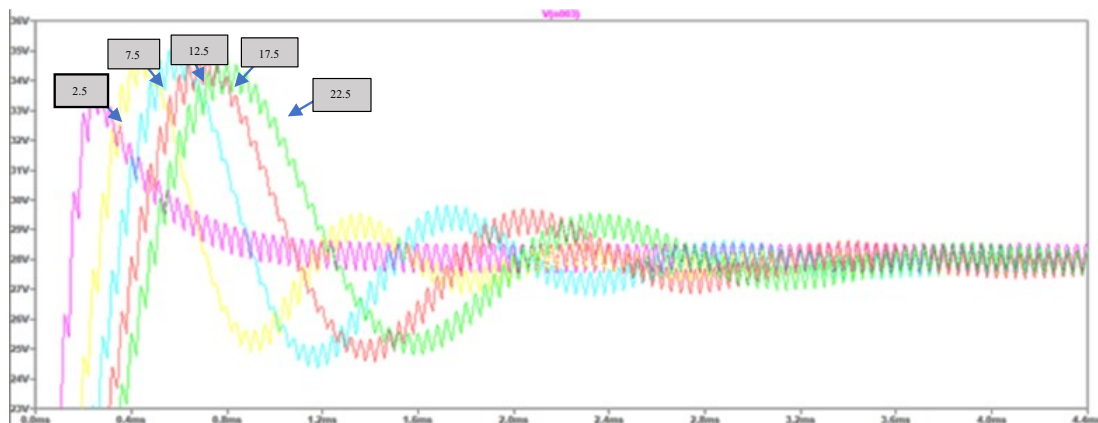


Fig. 5. Transient behavior with the variation of inductors as 2.5, 7.5, 12.5, 17.5 and 22.5 µH

Fig. 6 is a graph showing the inductor values, L , plotted against the peak output voltage, V_{Omax} . The peak voltage increases as the inductor value increases until a certain point, after which the peak voltage decreases with the increase in inductor value. This is due to a higher inductance reducing ripple current and thus increasing the maximum output current with the chosen integrated circuit.

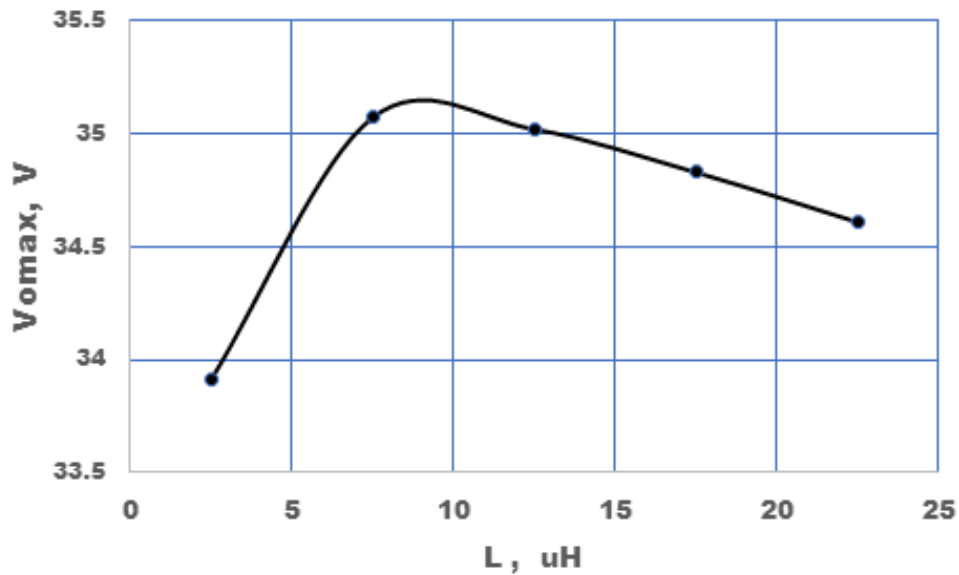


Fig. 6. The peak output voltage varies with the inductance variation during the transient state.

The transient peak also varies with the variation of the duty cycle, D. Figure 7 shows the variation of the peak voltage with the variation of the duty cycle and the output voltage. It is noted that the input voltage of the inverter also varies while changing the duty cycle to maintain the same output voltage. However, some variation in the output voltage was also observed.

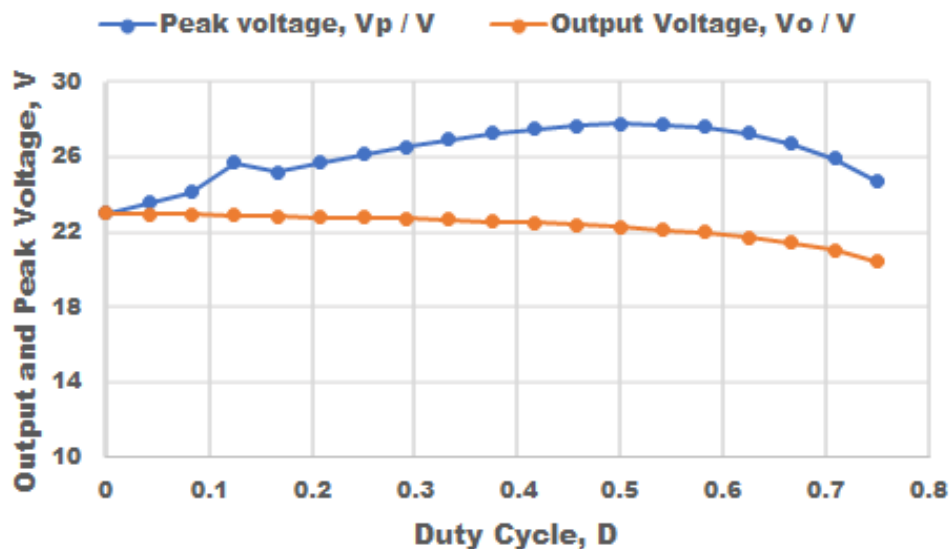


Fig. 7. Output and transient peak voltage phenomena with the duty cycle variation.

Table 1 shows the change in peak voltage, and output voltage, V_o , as the input voltage and duty cycle change. The formula used to calculate the duty cycle is:

$$D = 1 - \frac{V_i}{V_o}$$

Where, D – duty cycle, V_i – input voltage, V, and V_o – output voltage, V

To maintain the output voltage constant while the input voltage is decreased due to reducing solar output voltage, the duty cycle needs to be increased, as shown in Fig. 8. This figure shows a slight output voltage variation.

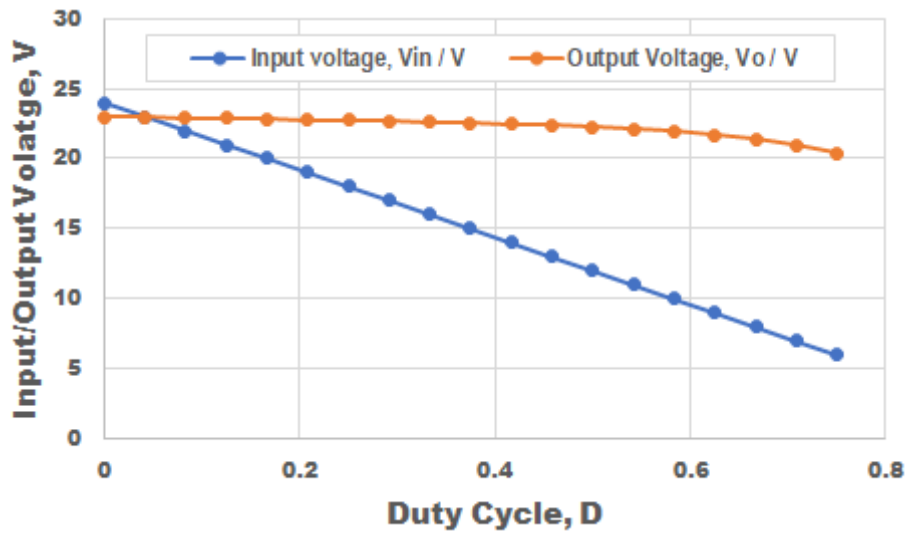


Fig. 7. Effect input voltage to maintain the constant output.

It can be seen that the duty cycle decreases as the input voltage is increased from 6V to 24V, while the output voltage, V_o , increases from 20.400 V to 22.977V

The simulation of the dual 555 timer is shown in Figure 8.

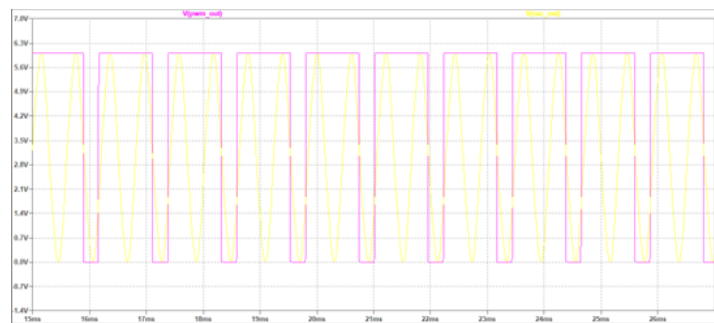


Fig. 8. Output voltage of the 555 timers

A 555 timer can generate a square-wave signal when set up like this. From the simulation, the voltage output for the oscillator (blue waveform) is changed to a square waveform at the PWM output.

To demonstrate the capabilities of an IC with Maximum Power Point Control, LTC3105 is being used. The simulation is shown in Figure 9.

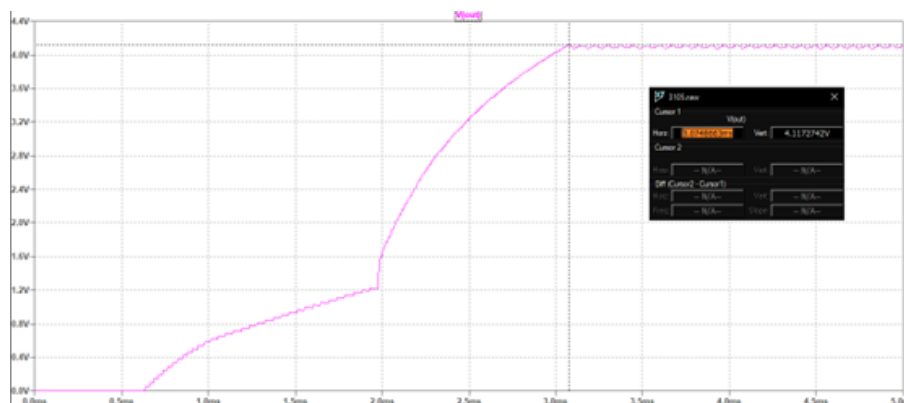


Fig. 9. Output voltage for the circuit of LTC3105

From the simulation, it can be deduced that the maximum power point for this circuit is reached at 3.07ms and when the voltage is 4.12V. This IC's maximum power point control (MPP) will constantly adjust the current or voltage depending on which of the two changes first so that the voltage output remains relatively constant.

Now, to compare the maximum power points, an equivalent solar cell circuit will be used, as shown in Fig.10.

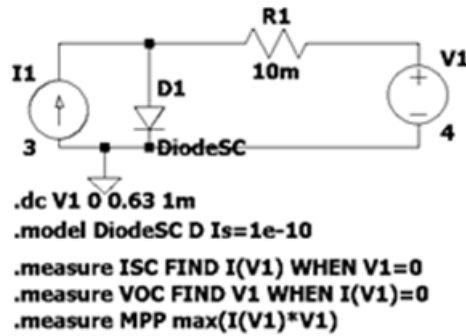


Fig. 10. Solar cell equivalent circuit

For this simulation, this circuit will be used to find its maximum power point (MPP). The MPP is the point on its current-voltage (I-V) curve where the product of current and voltage is at its maximum. Comparing this with the I-V simulation for the circuit shown in Figures 11 and 12 will prove that it aligns with the established theory.

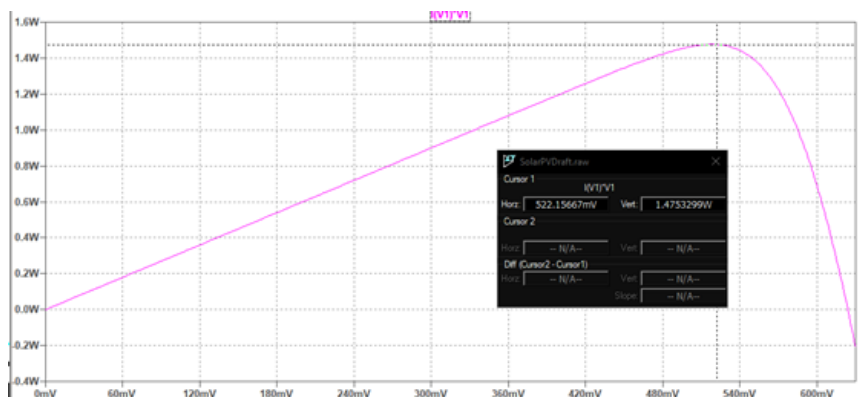


Fig. 7. I-V simulation graph showing the Maximum Power Point (MPP)

For a more detailed view of the short-circuit current, I_{sc} , and the open circuit voltage, V_{oc} , the data log for the simulation is shown in Figure 11.

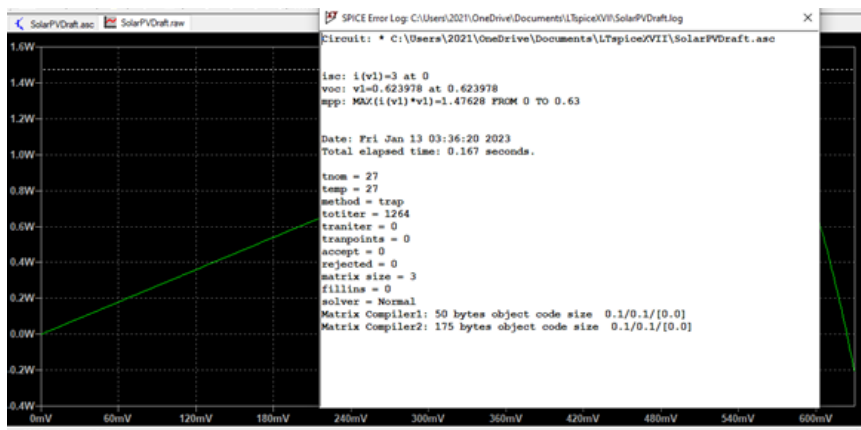


Fig. 8. Data log of the simulation

From Fig. 10, it can be deduced that the MPP is approximately 1.475W, and it reaches this value at 522.16mV. This is very close to a laboratory solar-cell voltage reading of 650mV. From the data log, the short circuit current, I_{sc} , is 3A, and the open-circuit voltage, V_{oc} , is 0.624V.

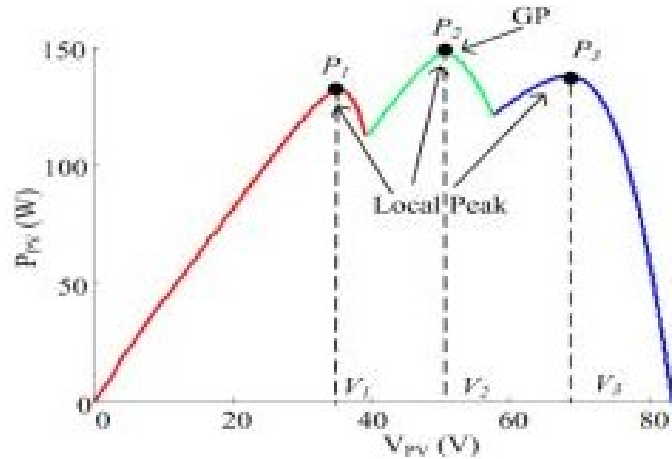


Fig. 9. PV curve for an entire array [5]

Comparing Fig. 12, taken from a research paper by Logeswaran & Senthil Kumar [5], which shows three power output peaks for the PV curve of an entire solar array, to Fig. 10, the maximum power output of Fig. 12 is about 150W (for peak, P2). The LTSpice simulation for a single solar cell is approximately 1.48W. Therefore, it can be concluded that at least 102 solar cells can be used to achieve the maximum power output of 150W.

5. CONCLUSION

This paper proposes a photovoltaic (PV) system utilising a Maximum Power Point Tracking (MPPT) algorithm by controlling the duty cycle of the inverter as one of the techniques to maximise the solar panel power output and the effect of the inductor for designing an inverter.

REFERENCES

- [1] <https://www.analog.com/en/products/lt8490.html> (accessed July 2022)
- [2] <https://www.analog.com/en/products/ltc4015.html> (accessed July 2022)
- [3] Elbarbary, Z.M.S. and Alranini, M.A. (2021), "Review of maximum power point tracking algorithms of PV system", *Frontiers in Engineering and Built Environment*, Vol. 1 No. 1, pp. 68-80. <https://doi.org/10.1108/FEBE-03-2021-0019>
- [4] U. U. Khan, M. Raheem, S. Ata, and Z. H. Khan, "Design and implementation of a low-cost MPPT controller for solar PV system," in *2016 International Conference on Open-Source Systems & Technologies (ICOSST)*, Lahore, Pakistan: IEEE, Dec. 2016, pp. 156–163. doi: 10.1109/ICOSST.2016.7838594.
- [5] T. Logeswaran and A. Senthil Kumar, "A Review of Maximum Power Point Tracking Algorithms for Photovoltaic Systems under Uniform and Non-uniform Irradiances," *Energy Procedia*, vol. 54, pp. 228–235, 2014, doi: 10.1016/j.egypro.2014.07.266.